Electrodeposition of Neodymium in the Room Temperature Ionic Liquid 1-Butyl-1-Methylpyrrolidinium Bis(trifluoromethylsulfonyl)imide and the Effects of Water and Ethanol: A Rotating Disk Electrode Study

A Thesis

Presented in Partial Fulfillment of the Requirements for the

Degree of Master of Science

with a

Major in Materials Science and Engineering

in the

College of Graduate Studies

University of Idaho

by

Jacob Kline

Major Professor: Batric M. Pesic, Ph.D.

Committee Members: You Qiang, Ph.D., Samrat Choudhury, Ph.D.

Department Administrator: Eric Aston, Ph.D.

May 2018

Authorization to Submit Thesis

The thesis of Jacob C. Kline, submitted for the degree of Master of Science with a major in Materials Science and Engineering and titled, "Electrodeposition of Neodymium in the Room Temperature Ionic Liquid 1-Butyl-1-Methylpyrrolidinium Bis(trifluoromethylsulfonyl)imide and the Effects of Water and Ethanol: A Rotating Disk Electrode Study," has been reviewed in final form. Permission, as indicated by the signatures and dates given below, is now granted to submit final copies to the College of Graduate Studies for approval.

Major Professor: _____ Date: _____
Batric M. Pesic, Ph.D.

Committee Members: _____ Date: _____
You Qiang, Ph.D.

_____ Date: _____
Samrat Choudhury, Ph.D.

Department
Administrator: _____ Date: _____
Eric Aston, Ph.D.

Abstract

Neodymium metal is widely utilized for its unique magnetic properties. Neodymium magnets are found in MRI machines, hybrid electric car motors, and in magnets that are required to operate at high temperatures. Neodymium is also found as a reaction product in spent nuclear fuels. In order to recycle these spent fuels, neodymium and other products must be removed. Due to its large electronegative deposition potential (~ -2.4 V vs SHE) traditional aqueous processes cannot be used as hydrogen evolution from water occurs prior to any metal deposition. Pyroprocessing techniques in high temperature molten salts require the arduous control of an inert atmosphere as well as the use of corrosive ions. Room temperature ionic liquids (RTIL's) provide a unique solution to these problems as these salts are liquid at room temperature and provide a wide electrochemical window (up to 5 V) for deposition of electronegative metals.

The goal of this study was to examine the electrochemistry and deposition morphology of neodymium metal in the RTIL 1-butyl-1-methypyrrolidinium bis(trifluoromethylsufonyl)imide (BMP-TFSI). BMP-TFSI is designed to be a hydrophobic RTIL for use in open atmosphere. This particular RTIL is stable in the cathodic direction up to -3 V vs Ag/AgCl which provided adequate stability to observe the deposition of neodymium metal. The rotating disk electrode technique was used to study the electrochemistry of neodymium, water, and ethanol in BMP-TSFI. Neodymium deposition was observed at -2.4 V and the morphology was characterized using scanning electron microscopy. The effects of water and ethanol additions to BMP-TFSI were also investigated to determine their effects on the stability of the RTIL. While BMP-TFSI is designed to be hydrophobic, moisture from the atmosphere can be absorbed in small amounts. Ethanol has been proposed as a viscosity modifier, to reduce the viscosity of ionic liquids. The diffusion coefficients of water and ethanol in BMP-TFSI were calculated to be 7.6×10^{-7} cm^2/sec and 1.8×10^{-9} cm^2/sec respectively. The reduction of ethanol on platinum in BMP-TFSI exhibited sluggish kinetics and the rate constant was calculated to be 4.3×10^{-4} cm/sec. Both water and ethanol additions drastically reduced the stability window of the RTIL to approximately 2 V.

Acknowledgements

I would like to thank the U.S. Department of Energy and their financial sponsorship of the project through the Nuclear Energy Universities Program. Grant Number #DE-NE00008556 (2016).

I gratefully acknowledge the invaluable guidance, training, teaching, and inspiration provide by my major professor Dr. Batric Pesic.

I also wish to thank my colleagues Ian Ehrsam, Robert Blair, and Sougat Singh for their valuable assistance and discussions throughout my time at the University of Idaho.

Dedication

This thesis is dedicated in part to my wonderful wife Morgan. Her constant encouragement was invaluable. I also want to thank my extended family, both in Idaho and in Alaska. Non Nobis.

Table of Contents

List of Figures

List of Tables

Chapter 1: Introduction

1.1 Basics of electrochemistry

The discipline of electrochemistry studies chemical reactions that involve the movement of electrons. The movement of electrons requires that one chemical species give up electrons, (oxidation), while another species receives the electrons (reduction). These reactions are commonly referred to as "redox" reactions. To illustrate this principle, consider the oxidation half-reaction of dissolved iron ions as seen below in Equation 1.

$$Fe^{2+} \rightarrow Fe^{3+} + 1e \qquad \text{Eqn. 1}$$

In Equation 1, iron is being oxidized from ferrous iron (Fe^{2+}) to ferric iron (Fe^{3+}) as the reaction proceeds to the right. The oxidation state of iron has increased from 2 to 3. Oxidation occurs when the oxidation state of the species moves to more positive numbers. Oxidation reactions occur at the anode in an electrochemical cell while reduction occurs at the cathode. An example of a reduction reaction is presented below in Equation 2 in the reduction of neodymium.

$$Nd^{3+} + 3e \rightarrow Nd^{0} \qquad \text{Eqn. 2}$$

In Equation 2 the oxidation state of neodymium has been reduced from +3 to 0, indicating that Equation 2 is a reduction half reaction. In both Equations 1 and 2, electrons are present as products and reactants respectively. To maintain charge neutrality in the electrolyte solution an equal and opposite half reaction must be also be occurring within the cell. The half reaction of interest is studied the working electrode, while the equal and opposite half reaction is driven at the counter electrode.

1.2 Thermodynamics of neodymium and the need for ionic liquids

For this thesis, the reaction of greatest interest is presented in equation 2, the reduction of trivalent neodymium to metallic neodymium. To bring the dissolved neodymium ions out of solution and create metallic neodymium, an electrochemical potential must be applied that

is more cathodic (i.e. more negative) than the standard reduction potential. Based on Table 1 below, this means that in order to deposit Neodymium metal, a potential more negative than -2.431 V must be applied.

Table 1.1: Standard reduction potentials for a variety of half-cell reactions. [1]	
Reaction	E^0 (V)
$Au^{3+} + 3e \leftrightarrow Au$	+1.498
$Cu^{2+} + 2e \leftrightarrow Cu$	+0.342
$2H^+ + 2e \leftrightarrow H_2$	**0.000**
$Ni^{2+} + 2e \leftrightarrow Ni$	-0.257
$Fe^{2+} + 2e \leftrightarrow Fe$	-0.447
$Al^{3+} + 3e \leftrightarrow Al$	-1.662
$Nd^{3+} + 3e \leftrightarrow Nd$	**-2.431**

Examining Table 1 closely indicates that electrodeposition of neodymium from aqueous solutions is impractical. This is because hydrogen will always be present in aqueous solutions and the generation of hydrogen gas from water should always occur before neodymium deposition can begin to occur. This observation indicates the need for a solvent with high conductivity and a large electrochemical window of stability. Solutions to this problem are found in molten salts.

1.3 Brief overview of ionic liquids and molten salts

It is important to distinguish between the terms “molten salts” and “ionic liquids.” Both can be technically defined as any salt that has been heated above its melting point. However in practice, the term “molten salts” typically refers to inorganic salts with melting points above 100° C. In contrast to these inorganic, high melting point salts, “ionic liquids” are typically comprised of at least one organic species (typically the cation) and have melting

points less than 25° C. For clarity in this manuscript the term “Room Temperature Ionic Liquid” or RTIL will be used.

One of the commonly used molten salts in electrochemistry is a eutectic mixture of lithium chloride and potassium chloride [2,3,4]. This mixture of approximately 45 mol% KCl and 55 mol% LiCl forms a low melting point eutectic, melting at 355 °C [5,6]. These high temperature molten salts provide good conductivity due to their completely ionic nature. High temperature molten salts also provide a wide electrochemical window due to the electrochemical stability of the potassium, lithium, and chlorine components. However, there are several disadvantages to processing in high temperature molten salts. Due to the high temperatures required often between 355° C and 550° C, energy costs can be large, especially on a commercial scale. The most significant drawback arises from the sensitivity of K, Li, and Cl to oxygen and moisture which requires that all processing be performed under a well controlled, inert atmosphere. These high temperature molten salts are also highly corrosive due to the lithium and chloride species present.

These deficiencies of high temperature molten salts led to the development of modern RTIL’s. RTIL’s are salts that are molten above 25° C as mentioned above. These salts are based on a bulky, organic cation such as the pyrrolidinium, imidazolium, or phosponium ions. These cations are paired with large anions which can be organic or inorganic. The large size and convoluted structure of these molecules help to prevent solidification of the salts at room temperature, leading to the low melting points. However, because of the size of these molecules, ionic liquids are typically very viscous, and as such the diffusion coefficients in ionic liquids are much typical than in aqueous solutions.

The first room temperature ionic liquids were reported by Henry Walden in 1914 [7]. These early ionic liquids were based on an ammonium cation and a nitrate anion. They were very moisture sensitive and as such were not suited for use in open atmosphere.Ionic liquids were revisited in the 1980’s when Wilkes et al. [8] synthesized an RTIL based on an imidazolium cation and chloroaluminate anion. Due to the sensitivity of the chloroaluminate anion to moisture, these first generation RTIL’s necessitated the use of controlled atmosphere. The advent of more moisture stable anions such as tretrafluoroborate (BF_4^-) and hexafluorophosphate (PF_6^-) brought about the second generation of ionic liquids. These ions

were less sensitive to moisture than their chloroaluminate predecessors but still adsorbed moisture from the atmosphere due to their hydrophilic nature. The advent of hydrophobic anions such as the TFSI anion made possible the use of ionic liquids in open atmosphere and led to surge of research interest in RTIL's as seen below in Figure 1.1.

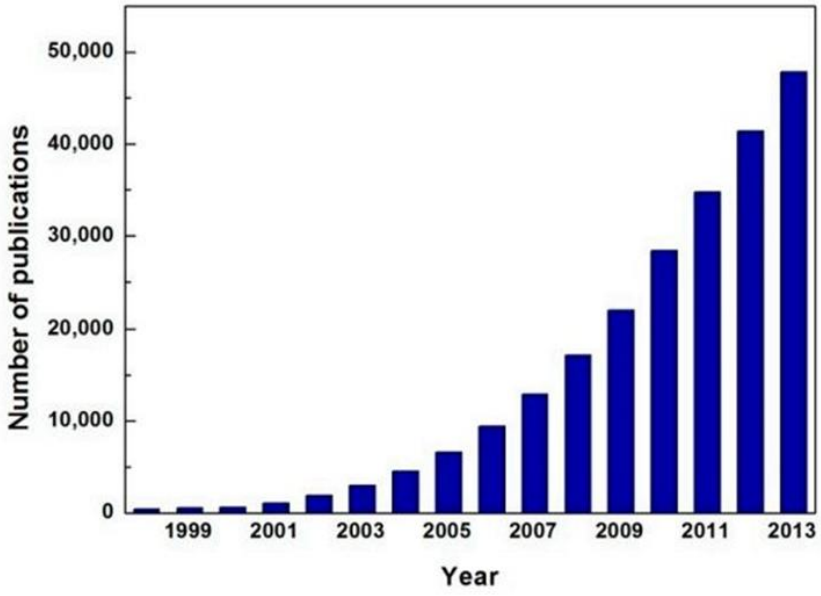

Figure 1.1: Number of publications concerning ionic liquids [9].

The use of RTIL's has skyrocketed in recent decades with the discovery of air and water ionic liquids as discussed above. Advances in organic chemistry have also provided a large range of cations and anions for use in RTIL synthesis as well as functional groups which can be added to provide specific properties. A sample of some common cations and anions are presented below in Figure 1.2. The addition of functional groups allows for the creation of tailor-made RTIL's. These functionalized ionic liquids are often referred to as task specific ionic liquids, and comprise the third generation of ionic liquids.

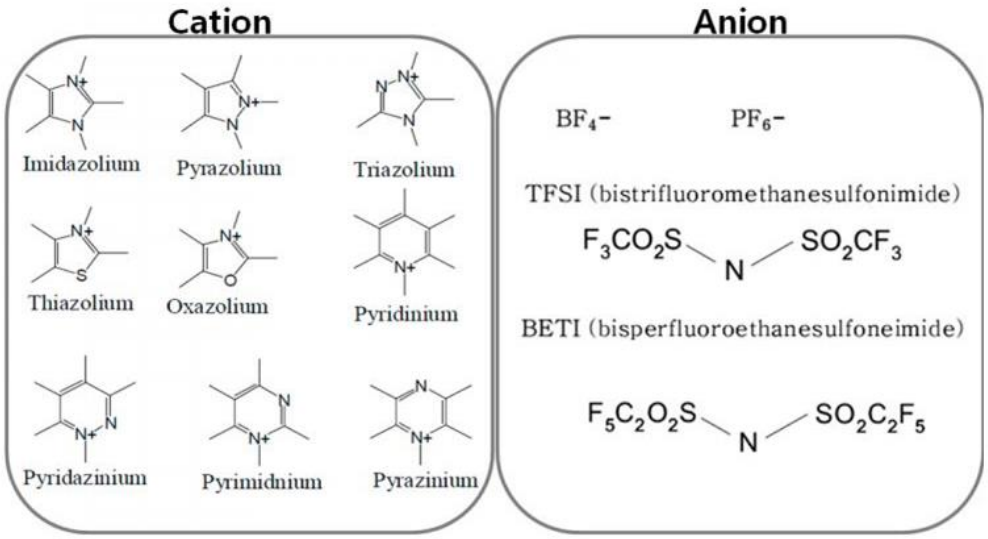

Figure 1.2: Chemical structure of some popular RTIL cations and anions [9].

Ionic liquids can also be described based on the acidity or alkalinity of their component ions. Neutral ionic liquids are based on anions that either neutral are very slightly basic in their acid/base behavior. A good example of a neutral anion is the TFSI anion, while the dicyanamide, lactate and acetate anions behave in a more basic fashion [10]. While the anion is responsible for the basic behavior of the RTIL, the cation is responsible for the acidity. The pyrrolidinum and imidazolium cations provide a weakly acidic behavior, as do early aluminum-chlorate ionic liquids.

For this work, the RTIL 1-Butyl-1-Methylpyrrolidinium Bis(trifluoromethylsulfonyl)-imide or BMP-TFSI was chosen as the electrolyte for its excellent electrochemical stability, particularly in the cathodic region. The chemical structure of the cations and anions of BMP-TFSI can be seen below in Figure 1.3. BMP-TFSI and current generation RTIL's provide chemical and physical properties that are well suited for uses in electrochemistry, batteries, sustainable chemical processing, and fuel cells to name just a few. RTIL's provide low vapor pressures, wide electrochemical windows, good thermal stability, and good electrical conductivity due to their entirely ionic composition [11,12].

(a) **(b)**

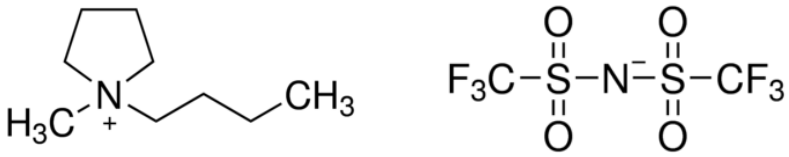

Figure 1.3: Chemical structure of the RTIL BMP-TFSI **(a)** BMP cation **(b)** TFSI anion.

1.4 Review of Current Knowledge of Lanthanide Electrochemistry in RTIL's

While complete summary of published literature on electrochemistry in RTIL's is beyond the scope of this thesis, the following section presents a brief review of electrochemical research in RTIL's with particular focus paid to the electrochemistry and electrodeposition of rare earth elements. Zhang et al. [13] reported electrodeposition of lanthanum from a DCA based ionic liquid. The researchers reported that their ionic liquid dissolved $NdCl_3$ through the formation of $Nd(DCA)_4^-$ complexes. These complexes were reduced at approximately -1 V vs Ag/Ag+ to form metallic lanthanum with nanoporous or nanoparticle morphologies. Nikitenko et al. [14] studied the behaviour of uranium chloride complexes in 1-butyl-3-methylimidazolium-TFSI and tri-n-butylmethyammonium-TFSI ionic liquids. A single three electron reduction step to metallic uranium was proposed at -3.1 V vs Ag/Ag+.Bhatt et al. [15] described the synthesis and CV response of a thorium (IV)-TFSI compound. They observed deposition of metallic thorium at -2.15 V with in a completely irreversible process. The researchers report that water was present as a contaminant from the synthesis process and they propose that the freshly deposited thorium film reacted chemically to form ThO_2 before the film could be oxidized electrochemically. Legeai et al. [16] reported the electrodeposition of lanthanum via a three electron step from the RTIL BMP-TFSI at a potential of -1.6 V vs an Ag/AgCl wire. SEM images confirm formation of lanthanum at -1.6 V and the researchers note that more cathodic deposition potentials led to poorly adhered and disordered films. Matsumiya et al. [17] studied the recovery of Nd, Pr, and Dy from an aqueous solution using a phosphonium based ionic liquid. They showed electrodeposition of Nd at -2.4V vs Fc/Fc+ with no intermediate reduction step. In a separate publication [18]

Matsumiya et al. examined the electrodeposition of Nd in a DEME-TFSA ionic liquid reporting a single, 3 electron transfer reduction step at -3.3 V vs Ag/Ag+. Chronoamperograms showed an instantaneous nucleation mechanism and semi-integral analysis of a cyclic voltammogram yielded a diffusion coefficient of 1.45 x 10^{-13} m^2s^{-1}. Chou and Hussey [19] studied the complexation of Nd (III) and Pr(III) in BMP-TFSI and found an initial single electron transfer step at around -1.5V vs Ag/Ag+.

Literature is scarce concerning the use of the rotating disk electrode technique to examine the electrochemistry of metals in ionic liquids, especially lanthanide elements. Pan and Hussey [20] studied the electrochemical and spectroscopic behavior of the trivalent lanthanides Sm, Eu, and Yb in BMP-TFSI. Using rotating disk voltammetry, they determined the diffusion coefficients for $Ln^{2+}/Ln^{3+}$and found them to be on the order of 1 x 10^{-10} cm^2s^{-1} for Eu and 1 x 10^{-7} cm^2s^{-1} for Sm and Yb. C. J. Rao et al. [21] studied Eu (III) in a BMP-TFSI system and reported the diffusion coefficient of Eu to be 3.1 x 10^{-8} cm^2s^{-1}. Yang et al. [22] studied the electrochemistry of Eu, Sm, Dy, and Nd in an imidazolium ionic liquid and found reduction peaks at approximately -0.6 V vs Ag/AgCl that they assigned to the first reduction step of the trivalent species to a divalent one. They reported diffusion coefficients on the order of 10^{-8} cm^2/s for Eu(III) and on the order of 10^{-10} cm^2/s for Sm, Dy, and Nd.

1.5 Statement of Research Goals

The objective of this research was to examine the electrochemistry of neodymium in the RTIL BMP-TFSI. Published literature provides conflicting information on the electrochemical processes involved in the electrochemical reduction of neodymium in ionic liquids.

It was also desired to understand the effects of water and ethanol impurities on the electrochemical stability and properties of BMP-TFSI. As the end goal of research in ionic liquids is to provide a low temperature, open atmosphere process for deposition of electronegative metals in ionic liquids, the role of water on BMP-TFSI should be understood. This is due to the fact that atmospheric moisture can be absorbed by RTIL's in spite of the hydrophobic design. Ethanol is a commonly used organic solvent and has been used in

literature as a dissolution agent for hard to dissolve salts in RTIL's. Ethanol has also been proposed as a viscosity modifier to decrease the relatively high viscosity of RTIL's.

Chapter 2: Electrochemical Techniques

2.1 Cyclic Voltammetry and Linear Sweep Voltammetry

Cyclic voltammetry (CV) is one the most popular techniques in electrochemistry. It is a powerful tool to examine the kinetic parameters and thermodynamics of homogeneous and heterogeneous electrochemical reactions [23]. CV is a potentiodynamic technique which involves scanning the applied potential from the initial potential towards a vertex potential. Once that vertex potential is reached the potential is returned to the starting potential, all at a constant potential scan rate. The current response to the applied potential is monitored. Cyclic voltammetry also provides critical information concerning the electrochemical reversibility of those reactions. In the discipline of electrochemistry, an electrochemical process is defined to reversible if the electron transfer processes (either oxidation or reduction) are fast enough that the system is constantly at equilibrium as the potential is scanned. For a completely reversible electrochemical system the separation between the peak potentials can be expressed as Equation 3 below at 25° C. In Equation 3, ΔE_p refers to the separation between the anodic and cathodic peaks. The terms $E_{p,a}$ and $E_{p,c}$ represent the anodic and cathodic peak potentials respectively, and n represents the number of electrons transferred.

$$\left|\Delta E_p\right| = \left|E_{p,a} - E_{p,c}\right| = \frac{0.059}{n} \qquad \text{Eqn. 3}$$

For a completely reversible system, the peak current values will scale linearly with the square root of scan rate and the peak potential will not change as a function of scan rate. Figure 2.1a presents a typical applied potential waveform for cyclic voltammetry. Figure 2.1b presents the current response to the applied waveform of Figure 2.1a.

(a) **(b)**

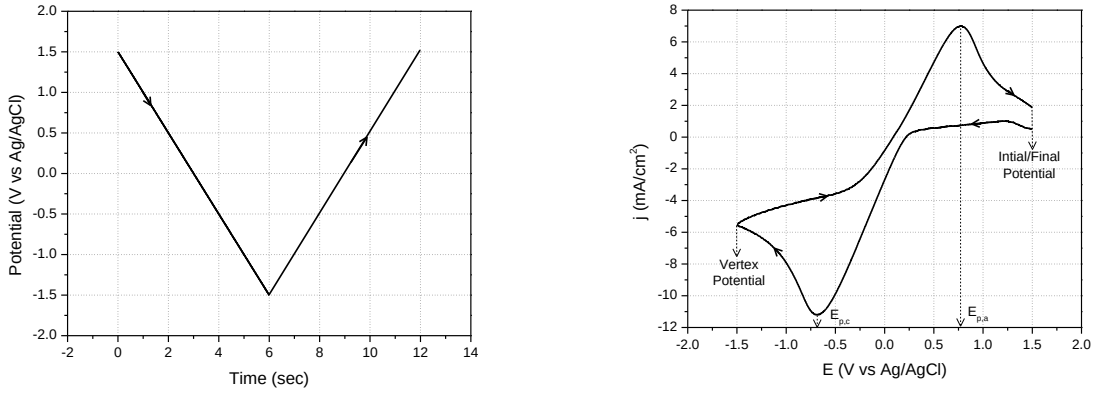

Figure 2.1: Representative CV figures**(a)** applied potential vs time waveform **(b)** resulting current density (current per unit area) response vs applied potential.

In the field of electrochemistry, the applied potential represents the applied driving force for the reaction, and the current response represents the resulting reaction rate. As the applied potential (driving force) reaches the level required by the thermodynamics for the particular reaction, the reaction will begin to proceed. As the driving force is increased further, the reaction rate will also increase up to a peak point. In a typical cyclic voltammogram these peak values will be present in the current response. These peaks are due to depletion of reactant(s) in the liquid boundary film. Once the concentration of species within the boundary film is depleted, the reaction must slow down and wait for mass transport through the boundary film to supply more reactant.

Linear sweep voltammetry (LSV) is a potentiodynamic technique that involves scanning the applied potential from a starting potential toward the final potential at a constant scan rate. This technique is very similar to a CV scan, except no return scan is performed from the vertex potential. A representative applied waveform for LSV is presented below in Figure 2.2a, and a current response is presented below in Figure 2.2b.

(a) **(b)**

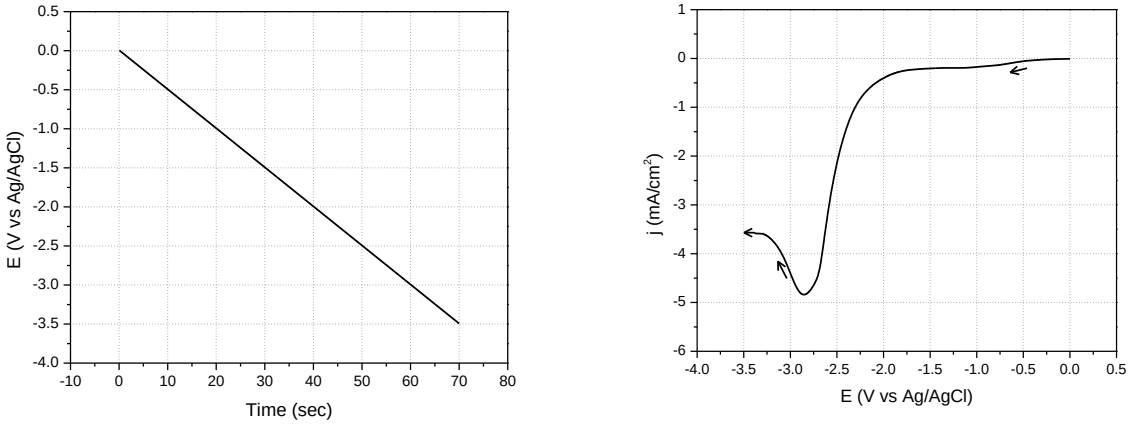

Figure 2.2: Representative LSV figures**(a)** applied potential waveform vs time **(b)** resulting current density vs applied potential.

Figure 2.2b demonstrates the current density response as the potential is scanned into the cathodic direction from 0 V to -3.5 V. As mentioned above, there is no return scan performed in LSV. LSV scans are particularly useful for imaging the electrode surface at particular points in the cathodic region seen during CV scans, without re-oxidizing and potentially altering the surface with a return scan in the anodic direction.

2.2 Chronoamperometry

In contrast to CV and LSV just discussed, Chronoamperometry (CA) is a potentiostatic electrochemical technique. In these experiments, the applied potential is held constant throughout the experiment, and the current response is measured as a function of time.

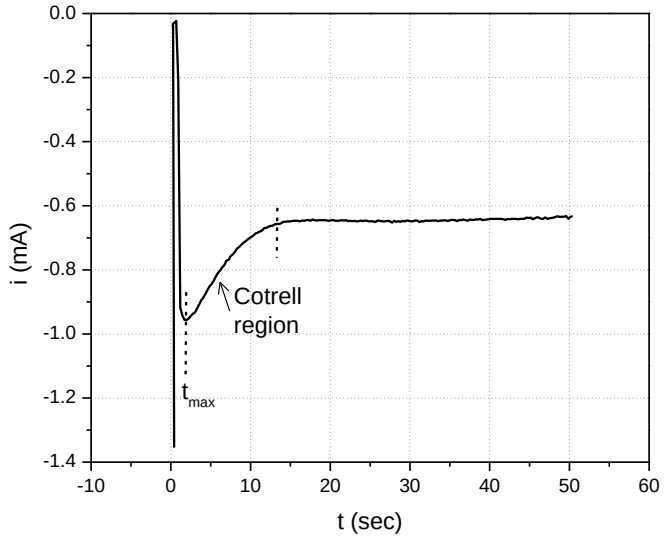

Figure 2.3: Representative CA experimental result with current plotted as a function of time with constant applied potential.

CA is a commonly used technique as it can provide information on the nucleation mechanisms of metals from solution. There are two possible mechanisms for metals to nucleate on a substrate. The first is by instantaneous nucleation, where metal atoms nucleate at the same time with the same size and grow at the same rate throughout the experiment. The second is by progressive nucleation, where metal atoms continue to nucleate throughout the experiment while others continue to grow leading to nuclei of different sizes. In the representative CA seen in Figure 2.3 the following features are observed. First, the large initial drop in the current value is due to the discharge of the chemical double layer on the electrode surface. Next the current increases up to the t_{max} value due to the nucleation of metal on the electrode surface. These nuclei provide increased surface area for the reaction to occur, thus the larger currents. And finally, after the t_{max} value, the nuclei grow large enough to overlap with one another and the surface area no longer increases. After this point the reaction is controlled by mass transfer and the current decays exponentially with time.

CA can also provide information on the diffusion coefficients and determination of the rate controlling mechanism (mass transfer vs reaction rate). This determination can by analysis with the Cottrell equation, presented below in Equation 4.

$$i = nFAC\left(\frac{D}{\pi t}\right)^{\frac{1}{2}} \qquad \text{Eqn. 4}$$

According to the Cottrell equation which was derived for purely diffusion controlled conditions; a plot of the current in the Cottrell region should be linear with respect to the inverse of time. The slope of the line contains the diffusion coefficient of the electroactive species.

2.3 Electrochemical Impedance Spectroscopy

In Electrochemical Impedance Spectroscopy (EIS), a DC potential baseline is applied to the working electrode. Typically, EIS experiments are run close to the equilibrium potential of the working electrode immersed in the solution. By using a small applied potential with respect to the equilibrium potential, several simplifications can be made in the analysis of the electrochemical responses. In contrast, the potentials applied in CV, LSV, and CA as discussed above are usually quite large, on the order of a few volts compared to the equilibrium potential. Once the DC baseline potential for EIS is chosen, a small AC perturbation is applied to that baseline potential. For the EIS presented in this work, a DC baseline potential of + 25 mV vs Ag/AgCl was used, in conjunction with a 5 mV AC potential magnitude. Once the baseline DC potential and the AC magnitude are set, the frequency of the AC oscillation is scanned over a range of frequencies. A typical frequency range at 10 kHz and runs to 10 mHz, with 5 points per decade scanned on a log scale. Once the experiments are completed the results can be plotted with the imaginary impedance on the Y-axis and the real impedance on the X-axis. This style of plot is known as a Nyquist plot. By calculating where the Nyquist plot intercepts the real impedance axis at high frequencies, the resistance of the solution can be determined.

2.4 Square wave voltammetry

Square wave voltammetry (SWV) is a potentiodynamic technique similar to cyclic voltammetry and linear sweep voltammetry already discussed. In square wave voltammetry the potential is stepped from an initial potential to a final potential with a given potential step size and. At each potential step a square wave of small amplitude is applied centered around the staircase potential. The current is sampled at the beginning and end of each potential step and the difference between them is commonly plotted as a function of potential. Sampling before and after the square wave potential is applied minimizes the contribution of the capacitive currents (due to charging) in favor of the faradic currents (due to reactions). Figure 2.4a below presents a typical applied SWV waveform and Figure 2.4b presents a typical response as provided by Mirceski et al. [24] in their review of the SWV technique.

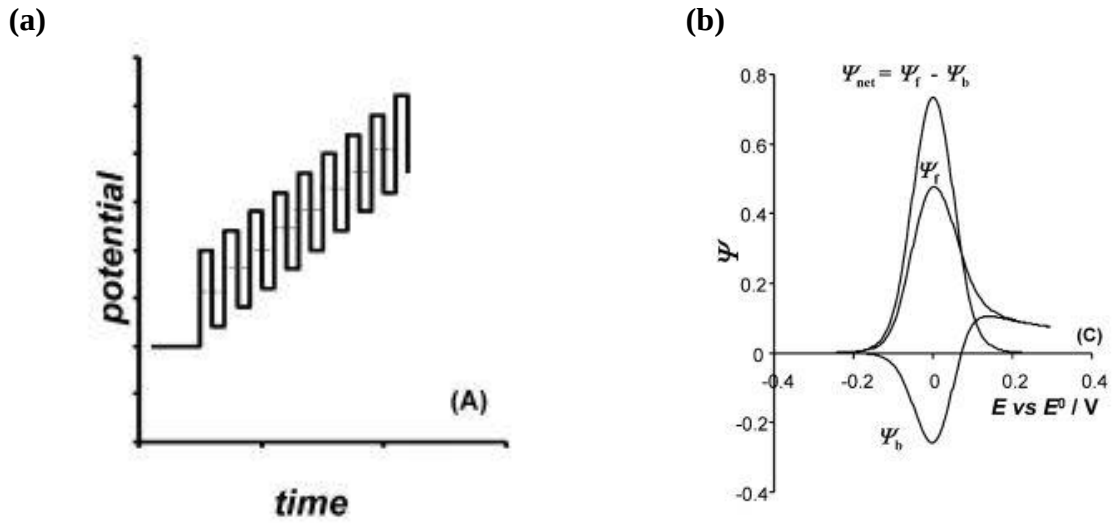

Figure 2.4: Representative SWV figures **(a)** applied potential waveform vs time **(b)** resultant current density vs applied potential. [24]

Notice that in Figure 2.4b that the dimensionless current ψ_{net} is the difference between the currents sampled before and after the square wave shape is imposed. As mentioned above, the technique of square wave voltammetry minimizes the capacitive currents in the system while still reporting the faradaic currents. For this reason, SWV is commonly used as

sensing technique to detect even very small amounts of pharmaceuticals or other contaminants.

2.5 Rotating Disk Electrochemistry

Rotating disk electrochemistry (RDE) is a particular branch of electrochemistry in which the working electrode is rotated in a controlled fashion. This controlled rotation varies the thickness of the liquid boundary film within the laminar flow regime. As the working electrode is rotated, the liquid boundary film is spun away from the electrode surface as a result of the centrifugal force. Solution from the bulk instantaneously replaces that which was swept away which decreases the thickness of the boundary diffusion layer. Diagrams provided by Nikolic et al. [25] are presented below in Figures 2.5a and 2.5b to illustrate this concept.

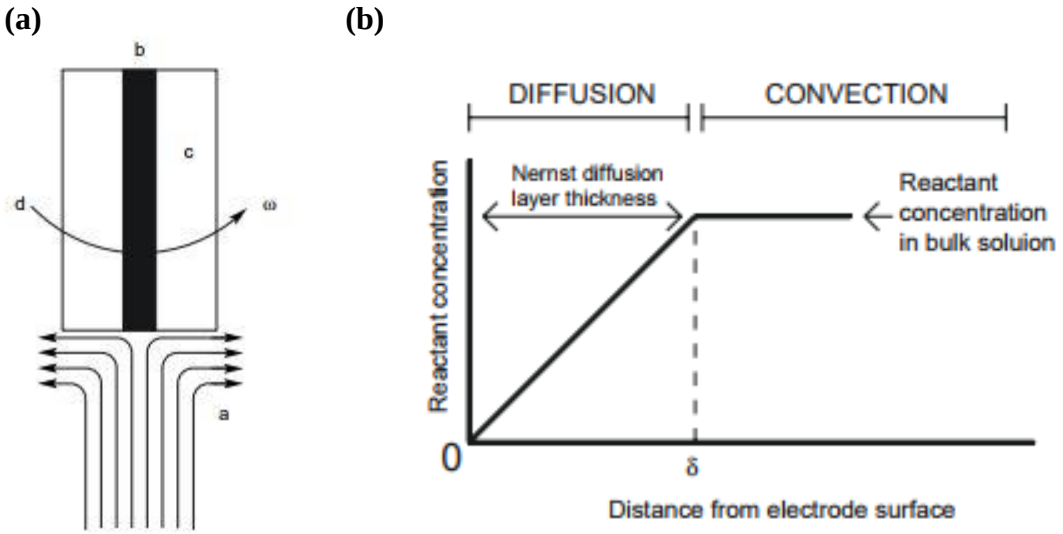

Figure 2.5: Effect of rotation on a disk electrode **(a)** solution movement caused by rotation of RDE **(b)** effects of rotation on thickness of diffusion layer. [25]

Figure 2.5a shows the motion of the fluid (a) as the electrode (b) and electrode sleeve (c) are rotated (d) with angular velocity ω. Fluid from the bulk replaces that which was spun away at the electrode surface. Increasing the rotation speed decreases the diffusion boundary

layer thickness seen in Figure 2.5b. A thinner diffusion layer leads to an increased concentration gradient between the electrode surface and the bulk electrolyte. The amount of diffusion through the boundary film is a function of the concentration gradient as given by Fick's 1st law, and as the concentration gradient increases, the rate of mass transport of reactants through the boundary film also increases. The fluid dynamics equations that govern the thickness of the boundary film were solved by the Russian scientist GrigorievichLevich and the famous Levich equation is presented below in Equation 5 [26].

$$i_{peak} = 0.62nFAD^{\frac{2}{3}}C\nu^{-\frac{1}{6}}\omega^{\frac{1}{2}} \qquad \text{Eqn. 5}$$

In the Levich equation *n* represents the number of electrons transferred, *F* is the Faradays constant, *A* is the electrode area, *D* is the diffusion coefficient of the electroactive species, *C* is the concentration of the species, *v* is the kinematic viscosity of the solution, and ω is the rotation speed of the electrode in radians per second. Notice from the Levich equation, that the slope of a plot of the peak current with respect to the square root of rotation speed should be linear and pass through the origin. The slope contains valuable information on the diffusion coefficient. Figures 2.6a and 2.6b below present experimental results based on the rotation disk electrode technique.

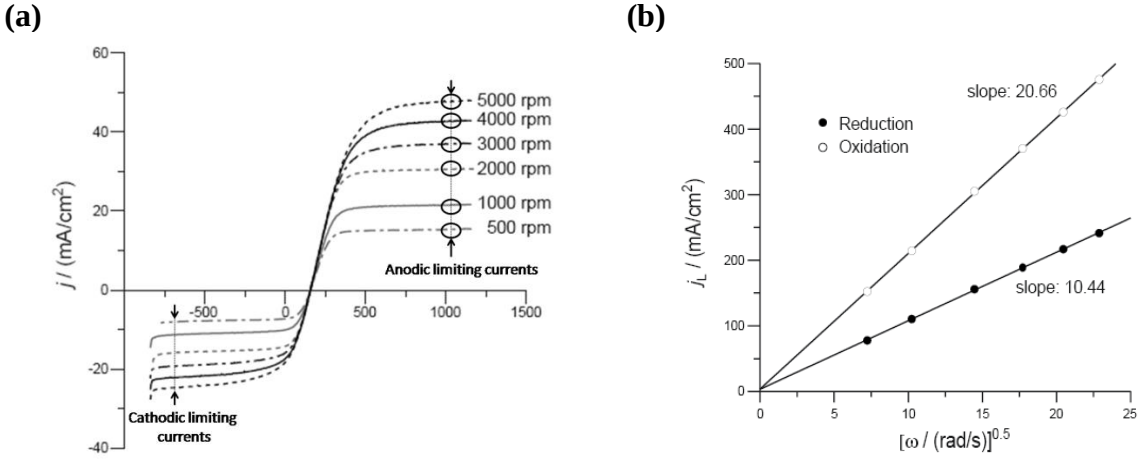

Figure 2.6: Experiment results from experiments using the rotating disk electrode technique **(a)** experimental voltammograms **(b)** Levich plot created using limiting anodic and cathodic currents seen in Figure 2.6a. Figures from Nikolic [25], with some annotations added.

Chapter 3: Experimental Setup

3.1 Electrochemical Cell

A standard three electrode electrochemical cell was used throughout this work. The three electrode cell consists of the working, reference and counter electrodes. This cell constructed by Dr. Batric Pesic [27] to require only small volumes of ionic liquid for electrochemical experimentation. The electrochemical cell is presented below in Figure 3.1.

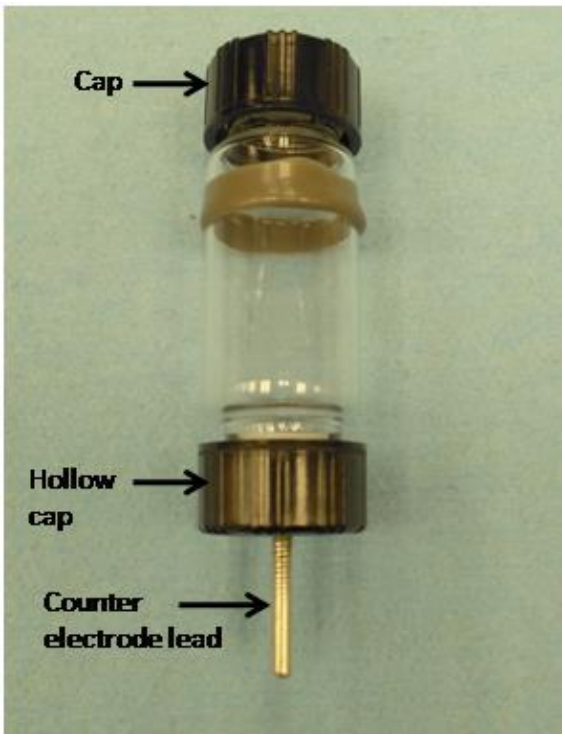

Figure 3.1: Three electrode electrochemical cells utilized for electrochemical tests. [27]

This cell design allowed for samples of less than 5mL volume to be easily studied. Experiments performed at room temperature were performed in the cell shown in Figure 3.1 with the shorter counter electrode stem. Experiments that were performed at elevated

temperatures required counter electrodes prepared with a longer stem to provide adequate length for clamping outside of the heating assembly.

3.2 Electrodes

3.2.1 Working Electrodes

In the three-electrode configuration, the working electrode is electrode on which the half reaction of interest is driven. In this work for example, the reduction of neodymium to metallic state as shown earlier in Equation 2 would occur on the working electrode. The general structures of the working electrodes used throughout this work are presented below in Figures 3.2a and 3.2b.

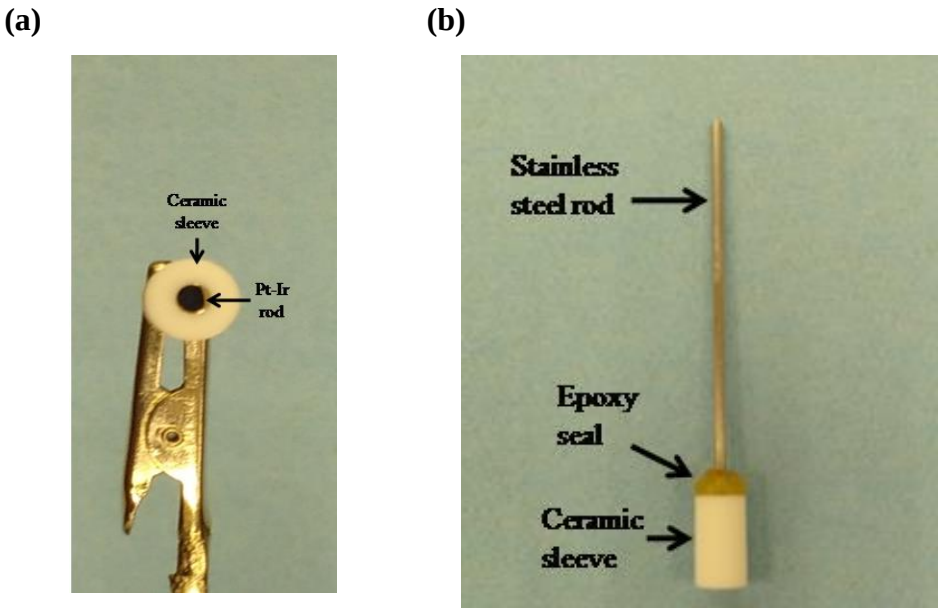

Figure 3.2: General structure of working electrodes utilized in electrochemical experiments **(a)** top down view of working electrode surface **(b)** side view of electrode.

For experiments involving rotation of the working electrode, the electrode connection was established by a spring-loaded graphite rod. The rod was pressed against the stainless

steel lead of the working electrode as seen in Figure 3.2a. This design provided excellent electrical contact throughout experiments with rotation.

3.2.2 Counter Electrodes

In the three-electrode electrochemical cell, the counter electrode provides the opposite half reaction as the working electrode in order to maintain the electrical neutrality of the solution. For example, if the half reaction being driven on the working electrode is the reduction of Nd^{3+} to Nd^{0}, the counter electrode must provide an equal and opposite (i.e. oxidation) reaction as seen in Equation 6 for the oxidation of chloride ions.

$$2Cl^{-} \rightarrow Cl_2 + 2e \qquad \text{Eqn. 6}$$

The counter electrode should be inert, in order to avoid generating any new soluble species that could interfere with the half reaction of importance being studied on the working electrode. In this work, graphite and platinum counter electrodes were used as can be seen below in Figures 3.3a and 3.3b.

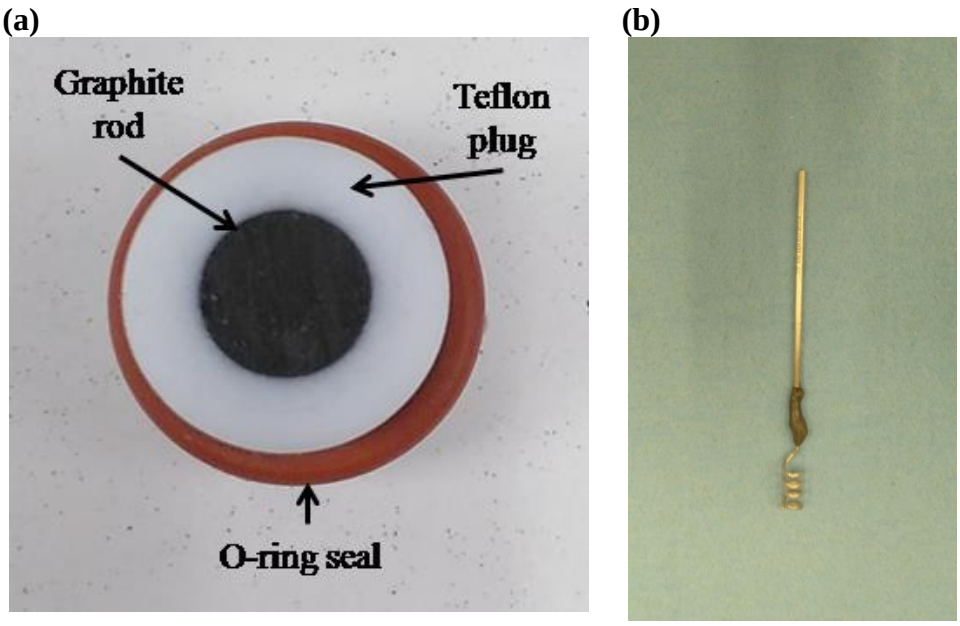

Figure 3.3: Counter electrodes utilized in the three-electrode electrochemical cell **(a)** graphite working electrode sealed in Teflon plug **(b)** platinum spiral counter electrode.

The graphite counter electrode was created by Dr. Batric Pesic [27] by machining out the Teflon tube just enough to insert the graphite rod while still maintaining a tight enough fit to prevent leakage of the ionic liquid. A lead wire was sealed to the bottom of the graphite rod using conductive epoxy. The lead can be seen protruding from the bottom of the electrochemical cells seen in Figure 3.1, and also below in Figure 3.4 which provides a better view of the counter electrode installation into the cell. The electrode was slid into the bottom of the electrochemical cell and the cap was tightened on to ensure a tight seal between the Teflon flange, O-ring, and cell wall.

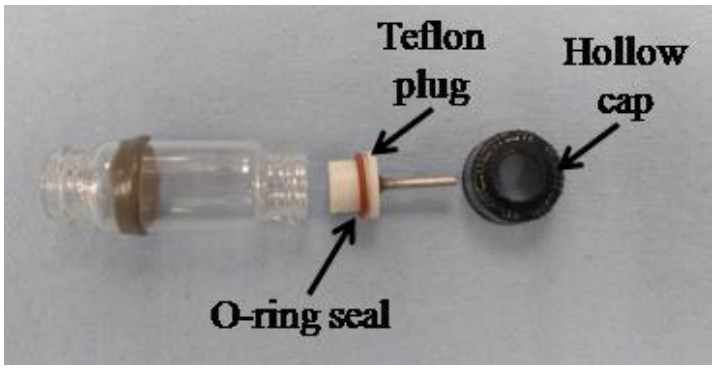

Figure 3.4: Example of electrochemical cell assembly. Counter electrode installs into bottom opening and is sealed with O-ring seal and tightened with the cap.

3.2.3 Reference Electrode

The reference electrode provides a stable, repeatable, half-cell potential against which the potential of the working electrode is measured. For this particular reference electrode, the Ag/AgCl couple is used for which the reaction is presented below in Equation 7 [1].

$$AgCl + e \leftrightarrow Ag + Cl^- \qquad E^0 = 0.222 \text{ V vs SHE} \qquad \text{Eqn. 7}$$

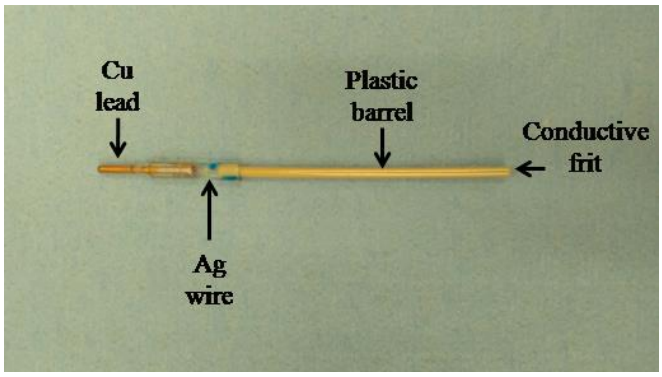

Figure 3.5: Ag/AgCl reference electrode utilized in electrochemical experiments.

Figure 3.5 presents the Ag/AgCl reference electrode used throughout this work. The electrode consists of a silver wire that was anodized in a 3M KCl solution to generate an AgCl layer on the silver wire. That wire was then placed into the plastic tube which was filled with 3M KCl. The end of the plastic tube was sealed with a conductive plug, which provides electrical contact with the solution, but prevents leakage of the electrolyte and contamination of the solution. The reference electrodes were checked daily against a Ag/AgCl master electrode and repaired or discarded if the potential difference was ever greater than 20 mV against the standard. The reference electrodes were also checked to ensure that the leak free status by repeatedly pressing the conductive plug against a paper towel. Even small leaks were easily detected by the color change of the paper towel.

3.3 Electrolytes and chemicals

BMP-TFSI >99% purity was procured from IoLiTec (Ionic Liquids Technologies, Tuscaloosa, AL, USA). Unless otherwise noted, all ionic liquid preparation was carried in the glove box under inert argon atmosphere. The ionic liquid was dried overnight at 80° C prior to use.

HTFSI >99% purity was procured from Tokyo Chemical Industry (Portland, OR, USA). All handling of HTFSI was performed in the glove box. HTFSI was dried at 80° C

prior to use. $NdCl_3$>99.99% (Arcos Organics) was dried under vacuum with heating prior to use.

Experiments using ethanol as a solvent required the use of absolute, 200 proof ethanol (Pharmco-AAPER, Mount Vernon, WA, USA).

3.4 Potentiostat

A CHI Instruments (Austin, TX, USA) model 760B potentiostat as seen in Figure 3.6 was used for all electrochemical experiments. The potentiostat was controlled by CHI Version 5.0.7 software.

Figure 3.6: CHI 760B potentiostat used for all electrochemical experiments.

3.5 Rotator

A Pitmman (Harleysville, PA) electrical rotator was for all experiments involving rotation of the working electrode. The shaft of the rotator was designed to fit into the metal sleeve allowing for easy removal of the rotator after experiments. A separate shaft within the metal sleeve transferred the rotation to the collet into which the working electrode was tightened. The rotator was controlled by EZServer HyperTerminal computer software allowing for precise control of the electrode rotation speed. The complete, rotator, sleeve, collet, and working electrode assembly can be seen below in Figure 3.7.

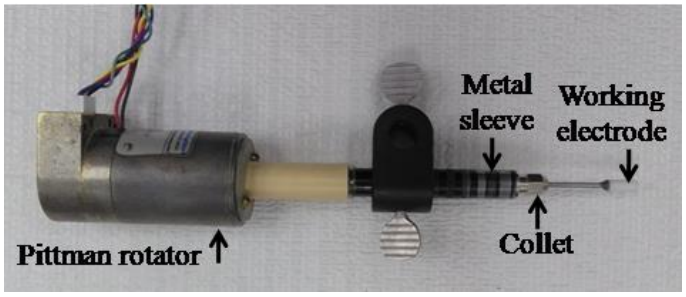

Figure 3.7: Rotator installed onto metal sleeve with working electrode installed into collet.

3.6 Complete experimental setup

Two pictures presenting the complete experimental setup for electrochemical experiments performed at room and high temperatures can be seen below in Figures 3.8a and 3.8b.

(a) **(b)**

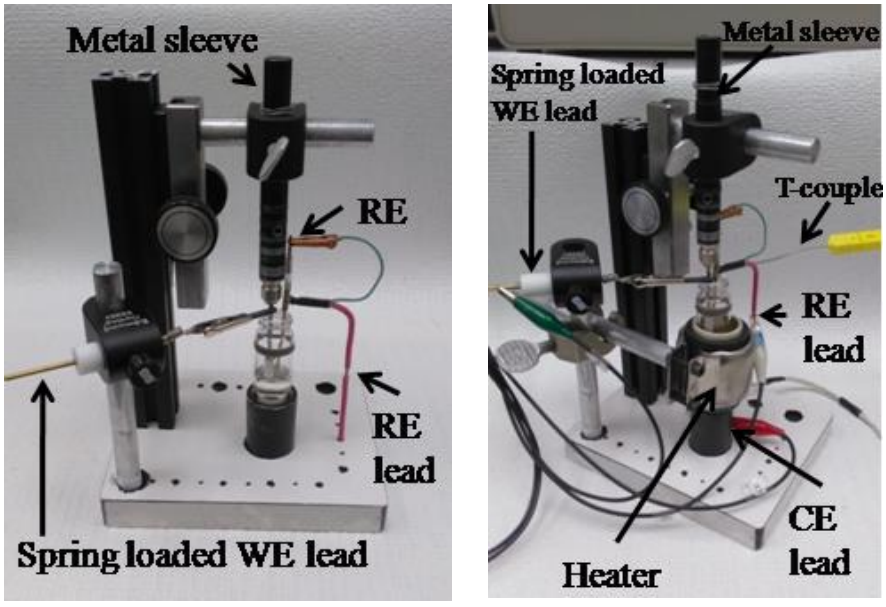

Figure 3.8: Complete electrochemical setups ready for experimentation. **(a)** room temperature setup **(b)** high temperature setup with heater and thermocouple added. [27]

Figure 3.8a presents the electrochemical setup used for experiments performed at room temperature. For experiments to study the effect of rotation speed, the analytical rotator as seen above in Figure 3.7 could be easily installed. Figure 3.8b presents the experimental setup with a heater added in order to perform experiments to determine the effects of temperature. Notice the heater and the thermocouple lead. This thermocouple was connected to a proportional temperature controller for accurate control of the temperature during experiments.

3.7 Scanning Electron Microscopy

A Tescan Vega II (Czech Republic) scanning electron microscope was used for all SEM characterization reported in this work.

Chapter 4: Electrochemical Results and Discussion

4.1 Validation of reference electrodes in BMP-TFSI

A stable and reproducible reference electrode potential is critical in electrochemistry. In ionic liquids in particular, the reference electrode is a particular challenge. Potentials in ionic liquids are commonly reported with respect to a quasi reference electrode which is often as simple as a platinum wire immersed in the solution to be studied. These quasi reference electrodes are difficult to reproduce between different solutions, and additives to the ionic liquids can significantly affect their stability. In our work, a specialized reference electrode was used. This reference electrode is shown above in Figure 3.5. The reference electrode was checked daily against a Ag/AgCl standard and was consistently accurate with less than 20 mV difference versus the standard.

(a) **(b)**

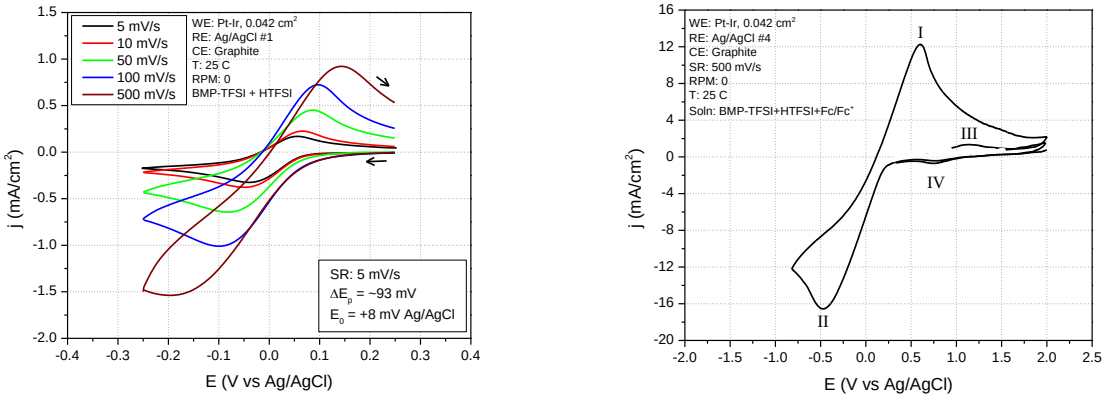

Figure 4.1: Cyclic voltammetry to determine the location of the hydrogen and ferrocene redox potentials in BMP-TFSI with respect to the Ag/AgCl reference electrode **(a)** BMP-TFSI with HTFSI added **(b)** BMP-TFSI with HTFSI and ferrocene added.

In order to establish the validity of the Ag/AgCl reference electrode in the RTIL BMP-TFSI, 421mg of HTFSI was added to 5g of BMP-TFSI to provide the hydrogen ion. Because

the anion was the same as that as the ionic liquid being studied, easy dissolution of HTFSI in BMP-TFSI was achieved. The addition provided free hydrogen ions which should be easily oxidized and reduced on a platinum surface. Figure 4.1a presents cyclic voltammograms in BMP-TFSI with HTFSI added to the ionic liquid. Notice the pronounced peaks centered around roughly + 8 mV versus our reference electrode for the scan performed at 5 mV/s. Increasing the scan rate as shown in Figure 4.1a leads to consistently increasing separation of the peak potentials indicating the redox reaction for hydrogen are quasi-irreversible. The redox reactions for hydrogen are presented below in Equation 8.

$$H_2 \leftrightarrow 2H^+ + 2e \qquad \text{Eqn. 8}$$

This observation of quasi-reversibility agrees well with those made by Bentley et al. [28] who studied the redox reactions of hydrogen in an imadazolium-TFSI ionic liquid, as well as Meng et al. [29] who studied the reactions of hydrogen on several metallic electrodes in an imadazolium RTIL.

Another commonly used standard recommended by IUPAC is that of the ferrocene/ferrocenium couple. Gange et al. [30] reported the use of the ferrocene/ferrocenium redox couple in an acetonitrile solution. The organic solvent acetonitrile prevents the use of typical aqueous reference electrodes. Gagne first studied the redox behavior of ruthenium in their solution, then added ferrocene and observed the redox potential of the new peaks. Torriero and Howlett [31] examined the standard potential of the ferrocene couple in several different ionic liquids, comparing it to decamethylferrocene, a more stable compound of ferrocene. The researchers report that the potential for the ferrocene couple varied over a range of roughly 100 mV in the variety of ionic liquids studied. In order to determine the reduction potentials of hydrogen and ferrocene with respect to our micro reference electrode, cyclic voltammetry was used to determine the location of the hydrogen and ferrocene redox peaks. Figure 4.1b presents a CV scan at 500 mV/s of BMP-TFSI with both HTFSI as well as ferrocene added to of 5g sample of BMP-TFSI. Notice again the pronounced peaks (designated as I and II) centered roughly around 0 vs the Ag/AgCl micro electrode. These peaks are again attributed to the redox reactions of hydrogen. It should be noted that there is significant peak separation of close to 1 V seen in Figure 4.1b compared to a separation of 400 mV as seen in the 500 mV/s scan as seen in Figure 4.1a. Two new peaks designated as

(III and IV) are seen in the scan around the potential of +1 V vs Ag/AgCl, separated by approximately 500 mV. These peaks were not seen in any previous experiments without ferrocene present, and are thus assigned to the ferrocene redox couple. It should be noted that this redox couple is centered at roughly +1 V compared to the Ag/AgCl reference electrode. This observation is in conflict with that made by O'Toole et al. [32] who reported that their ferrocene standard potential fell at approximately +320 mV/s with respect to a Ag/AgCl reference. It should be noted that O'Toole et al. used a 1 cm long ceramic frit which differs drastically in construction compared to the reference electrode used in the work presented in this manuscript. Another possible explanation for the shift and suppression of the ferrocene peaks is the interference of hydrogen species with the homogeneous reaction of the ferrous/ferric couple. Tang et al. [33] reported that an electrochemically generated TFSI radical contributed to the catalysis of hydrogen oxidation and reduction at specific sites on the electrode surface. Competition of ferrocene and hydrogen with one another could lead to the increased irreversibility for both species when both are present.

It should also be noted that multiple stability and reproducibility studies were performed which showed our Ag/AgCl reference electrode to be reproducible and stable in the room temperature ionic liquid BMP-TFSI. As discussed earlier, the reference electrode was checked daily versus a master standard and checked for solution leakage to ensure no contamination of the experimental solutions. With the validity of the Ag/AgCl reference electrode established with respect to reactions of hydrogen, rigorous electrochemical studies can be made in RTIL's without fear of unstable reference potentials.

4.2 Baseline CV scan of pure BMP-TFSI

The electrochemical window of BMP-TFSI is of critical importance, especially in the cathodic direction. The ionic liquid should demonstrate good stability without electrochemical degradation. As discussed above, the thermodynamics of neodymium reduction will require at least -2.5 V of stability in the cathodic direction. To determine the electrochemical window of BMP-TFSI, CV was used to locate the potentials at which BMP-

TFSI begins to break down on the platinum electrode. A baseline CV experiment is presented below in Figure 4.2.

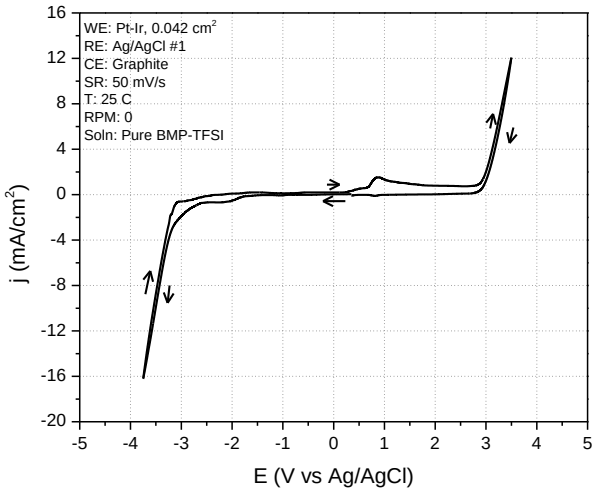

Figure 4.2: Baseline CV scan of pure BMP-TFSI.

Figure 4.2 demonstrates that BMP-TFSI has excellent stability in the cathodic region as the potential can be scanned to approximately -3.5 V vs Ag/AgCl before large currents are seen due to the electrochemical breakdown of the BMP cation. In the anodic direction the ionic liquid is stable up to +3 V vs Ag/AgCl, providing an impressive window of roughly 6 V of stability. With the baseline stability of BMP-TFSI established, further work to examine the effect of additives can be performed with confidence that the ionic liquid is stable between +/- 3 V vs Ag/AgCl.

4.3 Effect of water addition to BMP-TFSI

In order to understand the effects water additions on the electrochemical behavior of BMP-TFSI, incremental amounts of water were added to a 5 gram sample of BMP-TFSI. Because water has a far smaller electrochemical window than BMP-TFSI, cyclic voltammetry was used to examine the stability range of the ionic liquid as water was added. The CV's to

examine the effect of water addition are presented in Figure 4.3a. Figure 4.3b provides a simplified graph, demonstrating the extreme decrease in electrochemical stability of BMP-TFSI with a large amount of water present. Figure 4.3c presents LSV experiments to examine the effect of RPM on the reduction of water in BMP-TFSI on a platinum working electrode. Figure 4.3d presents a Levich plot generated from Figure 4.3c.

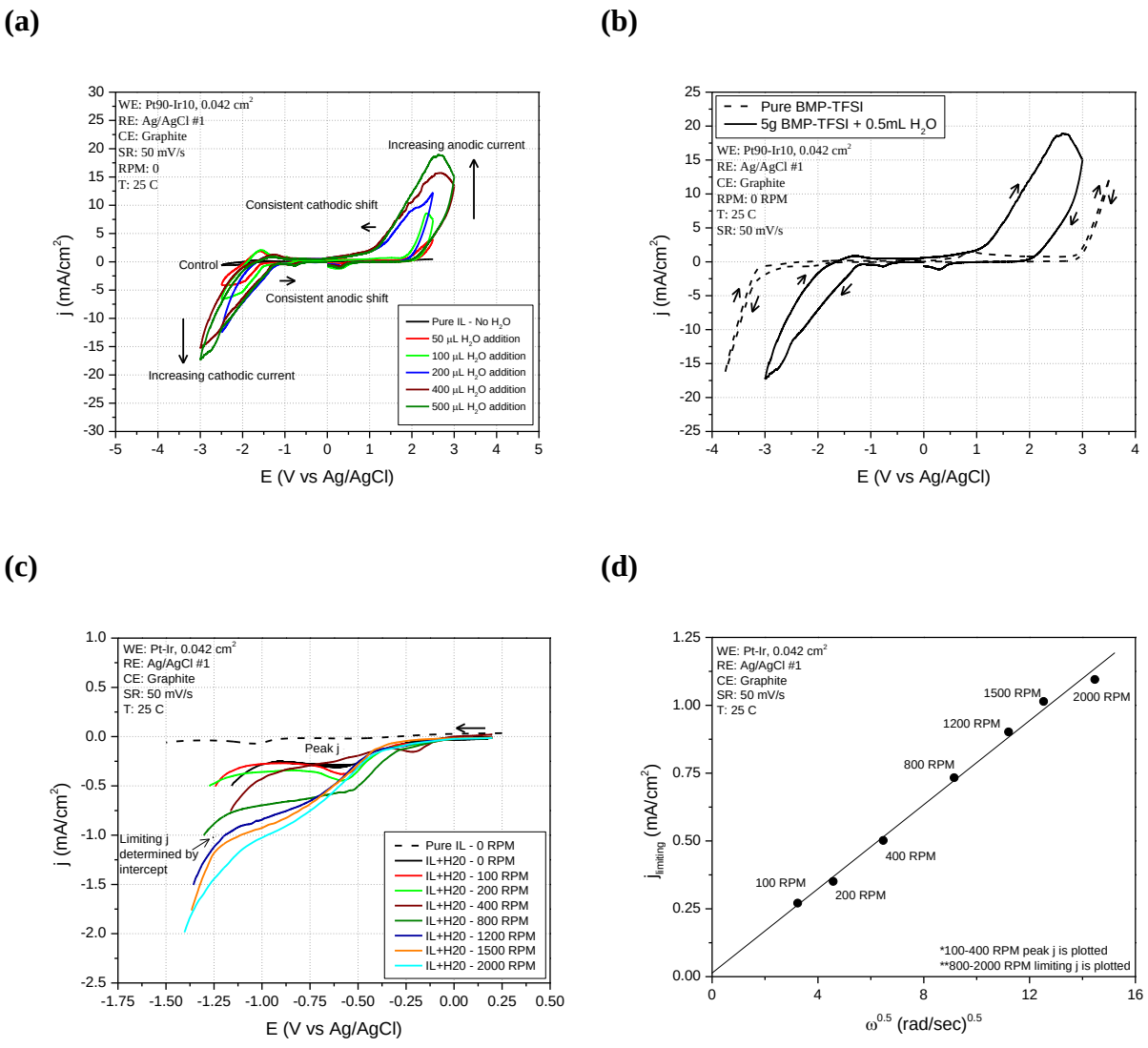

Figure 4.3: Electrochemistry of water in BMP-TFSI on a Pt working electrode **(a)** CV demonstrating effect of incremental addition of water to BMP-TFSI **(b)** CV to display effect of addition of 0.5 mL water to 5g BMP-TFSI **(c)** LSV in the cathodic region to examine effect of RPM effect on water reduction **(d)** Levich plot of limiting/peak cathodic currents as a function of rotation speed.

It is expected that addition of water to BMP-TFSI should decrease the electrochemical stability window as the added water can be split and hydrogen gas produced as seen below in Equation 9.

$$2H_2O + 2e \rightarrow H_2 + 2OH^- \qquad \text{Eqn. 9}$$

Figure 4.3a clearly demonstrates the decrease in electrochemical stability with increasing water additions. The first addition of 50 μL of water to ionic liquid decreases the cathodic breakdown potential from approximately -2.5 V to -1.5 V. Sequential additions of water produce a far smaller impact on the cathodic breakdown potential. This observation agrees well with the work of O'Mahony et al. [34] who studied the effects of water on the electrochemical windows of 12 RTIL's. Figure 4.3b presents a baseline, pure IL, CV scan along with a scan of the RTIL with 500 μL of water present. After additions of 150μL of water, a second aqueous layer was observed forming above the ionic liquid layer. O'Mahony observed a similar phenomenon, noting that the saturation water content of BMP-TFSI be 11,000 ppm with further addition of water resulting in an immiscible layer. Significant changes in the breakdown potential are not seen after 100-150μL water addition as this concentration roughly coincides with the saturation content of water in the ionic liquid. Above that concentration, water is excluded from the ionic liquid and forms an immiscible layer.

Examining the CV scans presented in Figure 4.3b closely reveals a peak or limiting current observed in scans with water added but not in pure ionic liquid. This peak is attributed to the splitting of water and generation of hydrogen gas. To further study these reactions, the rotating disk electrode technique was utilized in combination with linear sweep voltammetry. LSV scans to examine the effect of rotation speed are presented in Figure 4.3c. The pure ionic liquid scan reveals no significant peaks in the potential range from 0 to -1.5 V. When 500 μL of water added, distinct peaks and limiting currents are obvious. It should also be noted that the peak potential seen in Figures 4.3c correlate well with those seen in Figure 4.1b which were also attributed to the generation of hydrogen gas. For rotation speeds of 100, 200, and 400 RPM a peak current value is seen at approximately -0.6 V. However, with

rotation speeds above 400 RPM, the peak disappears and limiting currents are present in the scans up to the maximum measured rotation speed of 2000 RPM. This transition from peak to limiting currents should be attributed to the changing thickness of the liquid boundary film. For slow rotation speeds (100-400 RPM) the thicker boundary film leads to slow mass transport. As the water present in the boundary film is rapidly consumed, the current reaches a maximum value. As the supply within the boundary film is depleted, the reaction must wait for further reactant to diffuse through the boundary film and thus the current decreases from the maximum value. With faster rotation speeds above 400 RPM, the boundary film becomes thinner and thinner. As the boundary film becomes thinner, the mass transport through the layer is increased as required by Fick's 1st law. The increased mass transport allows the reaction to proceed faster without interruption, thus eliminating the peak and providing limiting currents.

The peak and limiting values seen in Figure 4.3c were plotted against the square root of rotation speed to produce a Levich plot which is presented in Figure 4.3d. The Levich plot demonstrates excellent linearity ($R^2 = 0.993$) up to the maximum studied rotation speed of 2000 RPM. Using the Levich equation as presented below in Equation 5, the diffusion coefficient for water in the RTIL BMP-TFSI was determined to be 7.6×10^{-7} cm^2/s. Notice again, that a plot of the peak current versus the square root of rotation speed should be linear and pass through the origin. The slope contains valuable information on the diffusion coefficient.

$$i_{peak} = 0.62nFAD^{\frac{2}{3}}C\nu^{-\frac{1}{6}}\omega^{\frac{1}{2}} \qquad \text{Eqn. 5}$$

For the calculation of the diffusion coefficient of water in BMP-TFSI the kinematic viscosity of the solution calculated to be 0.91911 cm^2/sec based on the work of Sanchez-Ramirez et al. [35]. For the concentration of water in BMP-TFSI, the saturation water content of ~11,000 ppm was used as reported by O'Mahony et al. [34]. This value is comparable to those reported by other researchers. Rollet et al. [36] measured the diffusion coefficient of water in an imadazolium-TFSI ionic liquid using pulse field NMR, reporting the diffusion coefficient of water to $2.6 \times 10^{-10} m^2/s$. Saihara et al. [37] reported the diffusion coefficient of water in imadozolium tetrafluoroborate to be 4.3×10^{10} m^2/s.

4.4 Effect of ethanol addition to BMP-TFSI

Ethanol is a commonly used organic solvent and is likely present in the ionic liquid as a residual contaminant from the synthesis process. Possible dissolution processes for difficult to dissolve metallic salts could involve the dissolution of salt in ethanol, then addition of the mixture to ionic liquid. Similar to water are described above, ethanol also possesses a far smaller electrochemical window than BMP-TFSI in the cathodic direction. The addition of ethanol to ionic liquid requires further study. Linear sweep voltammetry was used to determine the effects of ethanol addition on the electrochemical stability of BMP-TFSI in the cathodic region.

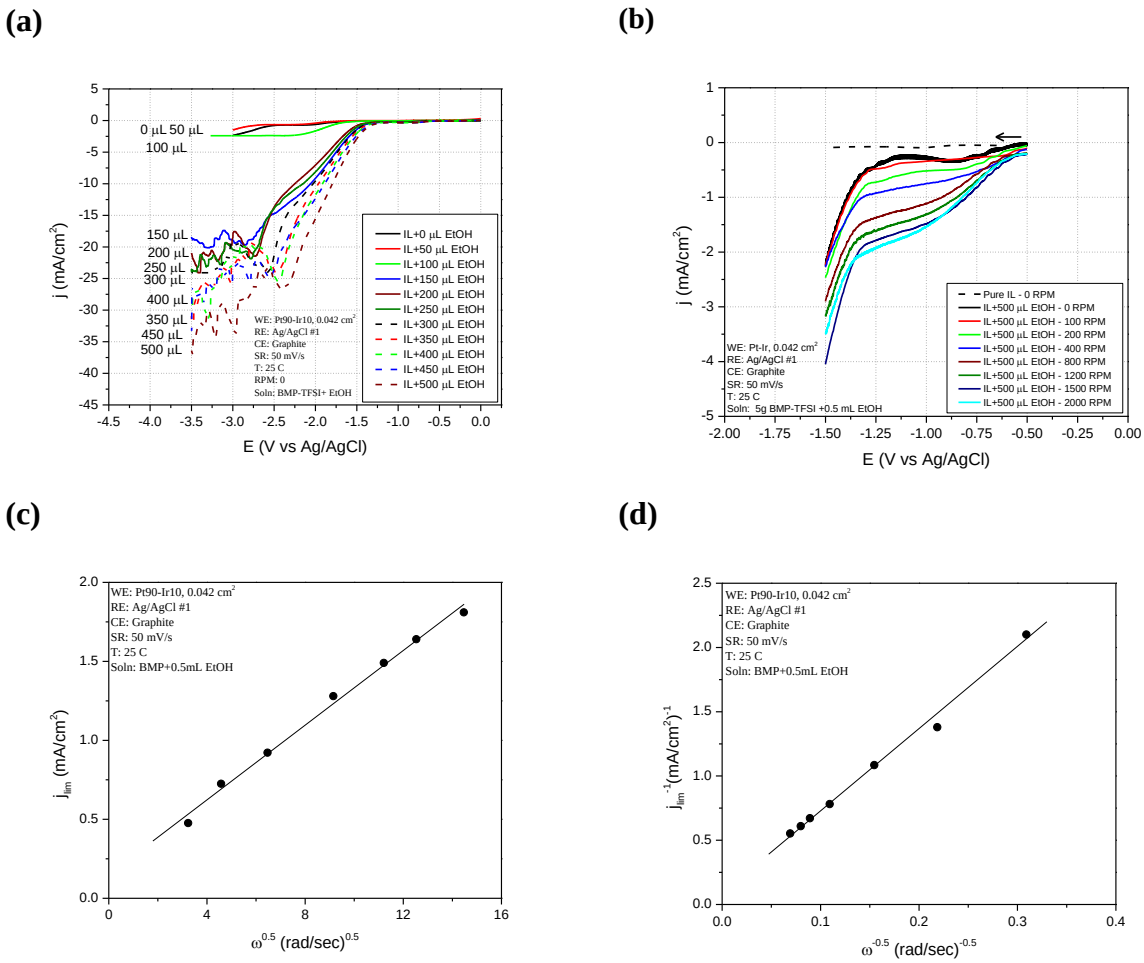

Figure 4.4: Electrochemistry of ethanol in BMP-TFSI on a Pt working electrode **(a)** LSV to examine effect of incremental ethanol additions to 5g BMP-TFSI **(b)** LSV in the cathodic region to examine the effect of RPM effect on 5g BMP-TFSI + 0.5mL ethanol **(c)** Levich plot of limiting/peak cathodic currents as a function of the square root of rotation speed **(d)** Koutecky-Levich plot of limiting/peak cathodic currents as a function of the square root of rotation speed.

Similar to water, ethanol has a far smaller window of electrochemical stability compared to ionic liquids. Figure 4.4a presents LSV in the cathodic region to examine the effect of incremental ethanol addition to ionic liquid. Notice from Figure 4.4a that additions of up to 100 µL of ethanol to a 5g sample of BMP-TFSI can be "tolerated" without a drastic change in the electrochemical stability. However, any further additions of ethanol results in a drastically reduced cathodic breakdown potential of roughly -1.5 V.

Schmidt et al. [38] studied the oxidation and reductions reactions of ethanol on platinum and ruthenium electrodes and alloys. The researchers extensively studied the electrochemical reaction products of ethanol on platinum and ruthenium using mass spectroscopy. Using mass spectroscopy, they identified ethane and methane gasses as the primary reduction products of ethanol produced on platinum. A two step reduction process for ethanol was proposed and demonstrated by the authors as presented below in Equations 10 and 11. The first step in the reduction process was the adsorption of ethanol or an ethanol radical (negatively charged ethanol molecule) onto the platinum surface (Eqn. 10).

$$CH_3CH_2OH + e \rightarrow CH_3CH_2OH^-_{adsorbed} \qquad \text{Eqn. 10}$$

Once the ethanol molecule or radical was adsorbed, it was reduced to ethane or methane gas depending on whether or not the carbon-carbon bond was broken during the reduction process (Eqn. 11). The authors [38] note that the splitting of the carbon-carbon bond is not likely on a platinum surface as platinum does not serve as a good catalyst for the breaking of carbon-carbon bonds, and as such this possible reaction is ignored.

$$CH_3CH_2OH^-_{adsorbed} + e + 2H^+ \rightarrow CH_3CH_3 + H_2O \qquad \text{Eqn. 11}$$

If the C-Cbond remained intact, the adsorbed molecule was reduced to ethane gas. If the bond was broken, ethanol would be reduced to methane gas. The oxidation products of ethanol on platinum were reported by Schmidt et al. to be CO_2 gas primarily.

Similar to water, a region of distinct limiting currents can be seen around -1.2 V. Figure 4.4b presents LSV to examine the effect of RPM on a 5g BMP-TFSI samples with 500μL of ethanol added. A consistent increase in the limiting currents is seen with increasing rotation speed. As discussed above, this observation is understood by the increasing rotation speed decreasing the thickness of the liquid boundary film and driving faster mass transport to the electrode surface. The Levich plot shown in Figure 4.4c again shows excellent linearity ($R^2 = 0.992$). However, unlike the Levich plot seen in Figure 4.3c, a distinct, non-zero, intercept is seen in Figure 4.4c. This observation indicates that there is a sluggish kinetic parameter which must be taken into account. In order to determine the diffusion coefficient and the reaction rate constant, the Levich-Koutecky equation must be used as seen below in

Equation 12, where the new term i_k represent the current that would be expected without any diffusion control.

$$i_{peak}^{-1} = \frac{1}{i_k} + \left(\frac{1}{0.62nFACD^{\frac{2}{3}}\nu^{-\frac{1}{6}}}\right)\omega^{-\frac{1}{2}} \qquad \text{Eqn. 12}$$

Examining the Levich-Koutecky equation reveals that a plot of inverse limiting current versus the inverse of square root of rotation speed should be linear. In this type of plot, the slope contains information on the diffusion coefficient while the intercept contains information on the reaction rate constant. Figure 4.4d presents a Levich-Koutecky plot to determine the kinetic parameter. Again, excellent linearity is seen in the Levich-Koutecky plot, and a distinct intercept is seen. By utilizing the Levich-Koutecky equation presented above in Equation 12, the diffusion coefficient of ethanol in BMP-TFSI was determined to be $1.8x10^{-9}$ cm^2/s and the reaction rate constant for ethanol reduction on platinum was calculated to be $4.3x10^{-4}$ cm/s. For calculation of the Levich-Koutecky equation, the same viscosity value was used as previously described for the calculation involving water. As ethanol and BMP-TFSI are completely miscible, the concentration was calculated based on the addition of 0.5 mL of ethanol to 5g of BMP-TFSI.

4.5 EIS to examine effects of water, ethanol, and $NdCl_3$ addition on solution conductivity

Due to their completely ionic nature, RTIL's are known to have good solution conductivity [39,40,41]. In addition to affecting the electrochemical stability as shown above for water and ethanol, ethanol and water have also been shown to influence the conductivity of ionic liquid solutions. Li et al. [40] studied the effects of organic molecular solvents on the conductivity of imadazolium based ionic liquids and found the solution conductivity increased with addition of the solvent. The authors attributed this increase to the increased mobility of charge carrying ionic liquids species as the molecular solvent decreased the solution viscosity. Widegren et al. [42] studied the effects of water additions to ionic liquids and found a similar trend of increasing conductivity with water addition. To study the effects of water, ethanol, and metal salt additions to our pyrrolidinium based RTIL, EIS experiments were performed at

room temperature in open atmosphere. Nyquist plots are presented below in Figure 4.5 and table of calculated solution conductivity values is presented in Table 4.1.

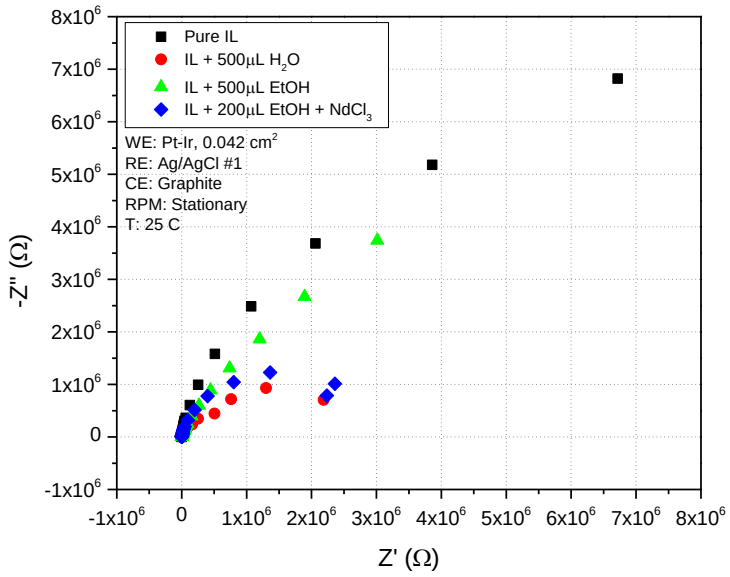

Figure 4.5: Nyquist plots to examine the effects of additives on the solution conductivity of BMP-TFSI. Solutions studied: 5g pure IL, 5g IL + 0.5mL H_2O, 5g IL + 0.5mL EtOH, 5g IL + 0.2mL EtOH + 125mg $NdCl_3$.

Table 4.1: Calculated solutionresistance and solution conductivity values from EIS data.

Solution	Resistance (ohms)	Conductivity (mS/cm)
Pure BMP-TFSI	725	6.9
BMP-TFSI + 500µL H_2O	247	20.2
BMP-TFSI + 500µL EtOH	894	5.6
BMP-TFSI + 200µL EtOH + $NdCl_3$	478	10.5

By extrapolating the high frequency intercept of the Nyquist plots with the real impedance axis, the solution resistance can be determined. Using this method, the values of the solution conductivity were calculated for the four different samples of ionic liquid. The results are tabulated in Table 4.1. For pure BMP-TFSI the solution conductivity agrees fairly

well with the value of 3.93 mS/cm reported by Sanchez-Ramirez et al. [34]. The larger value in pure BMP-TFSI could be due to a small amount of moisture absorption from the atmosphere as these experiments were conducted in open atmosphere. With addition of water, the solution conductivity is greatly increased, attributed to decreasing solution viscosity as described by Widegren [42]. The smaller solution viscosity allows for greater mobility of charge carriers and thus to increased conductivity. With the addition of ethanol to the pure ionic liquid, a slight decrease was seen in the solution conductivity. This is in contrast to the data reported by Zhang et al. [43] who reported increasing conductivity with increasing ethanol addition up to a point for their ionic liquids based on the pyrridinium cation. Tshibangu et al. [44] also reported increasing conductivity with methanol addition their imadozolium based RTIL. Ethanol is known to be both polar and non-polar in its behavior, and as such should contribute slightly to the solution conductivity with its polar OH group. Its non-polar behavior is seen on one end of the molecule terminated in the CH_3. However, the other end of the molecule with the OH group exhibits polar behavior due to the large difference in electronegativities between oxygen and hydrogen. With neodymium chloride present via ethanol addition, a marked increase in the solution conductivity is noticed. Addition of neodymium chloride provides an increased number of charge carriers to increase the solution conductivity.

4.6 Square Wave Voltammetry – Effect of additives to BMP-TFSI

Square wave voltammetry combines the capabilities of cyclic voltammetry with the increased sensitivity of pulsed potential techniques. To the study the effects of water, ethanol, and neodymium chloride additions to BMP-TFSI, the following square wave voltammetry experiments were performed, shown below in Figure 4.6.

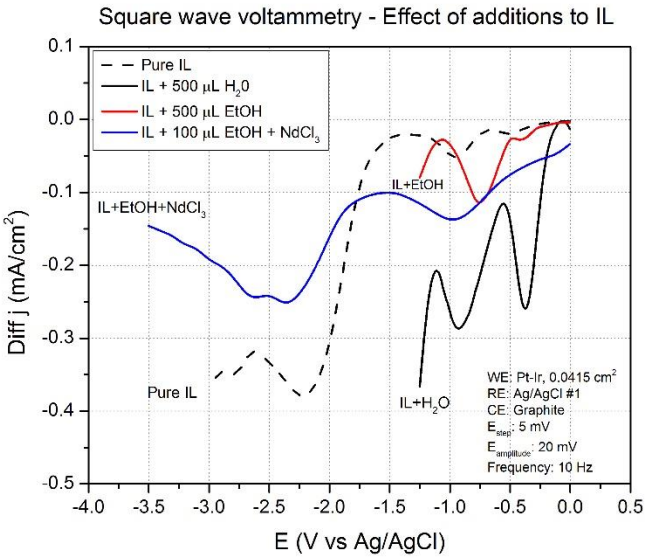

Figure 4.6: Effect of additives on the square wave voltammograms of BMP-TFSI. Solutions studied: 5g pure IL, 5g IL + 0.5mL H_2O, 5g IL + 0.5mL EtOH, 5g IL + 0.2mL EtOH + 125mg $NdCl_3$.

Notice in the scan performed in pure BMP-TFSI, the presence of two small peaks in the range of 0 to -1.5 V. A much larger cathodic peak is seen occurring at approximately -2.25 V. The two smaller peaks coincide very closely with the location of the peaks seen in the scan with water added to the ionic liquid. The presence of these peaks in pure ionic liquid could be explained by absorption of small amounts of moisture from the open atmosphere. As mentioned above, linear sweep voltammetry is a very sensitive technique and could be capable of detecting these trace amounts of moisture in BMP-TFSI. The scan with ethanol only added presents a single peak at a distinct potential compared to the two separate peaks seen with water only added. The scan with neodymium chloride present provides no new distinct peaks to be attributed to the reduction of neodymium in BMP-TFSI. One of the

primary used of square wave voltammetry is to calculate the number of electrons transferred during a reversible electrochemical reaction. However, as discussed above in Figures 4.1a and 4.1b, even the redox reactions of hydrogen are commonly quasi-irreversible in the BMP-TFSI ionic liquid system. In comparison with the redox reactions of hydrogen, the reactions of neodymium are likely more complex and will tend towards irreversibility. As such, square wave voltammetry is ill-suited to use for quantitative determination of the number of electrons transferred in this ionic liquid system.

4.7 Effect of IL addition to ethanol solutions without neodymium present

While previously the effects of ethanol additions to BMP-TFSI were studied, further work was performed to understand the reactions of ethanol in BMP-TFSI. For the following set of experiments, small amounts of ionic liquid were added to a 5g sample of ethanol. The addition of ionic liquid will provide solution conductivity to the ethanol solution. Ethanol itself, due to its partly non-polar nature, is unable to provide charge carrying species to contribute to conductivity. With little to no solution conductivity in pure ethanol, no reactions are expected. However, incremental addition of completely ionic BMP-TFSI provides charge carrying species which help to complete the electrical circuit between the counter and working electrodes. Cyclic voltammetry was used to examine the effects of incremental BMP-TFSI addition to pure ethanol, as well as the effects of scan rate and a rotation speed of 400 RPM.

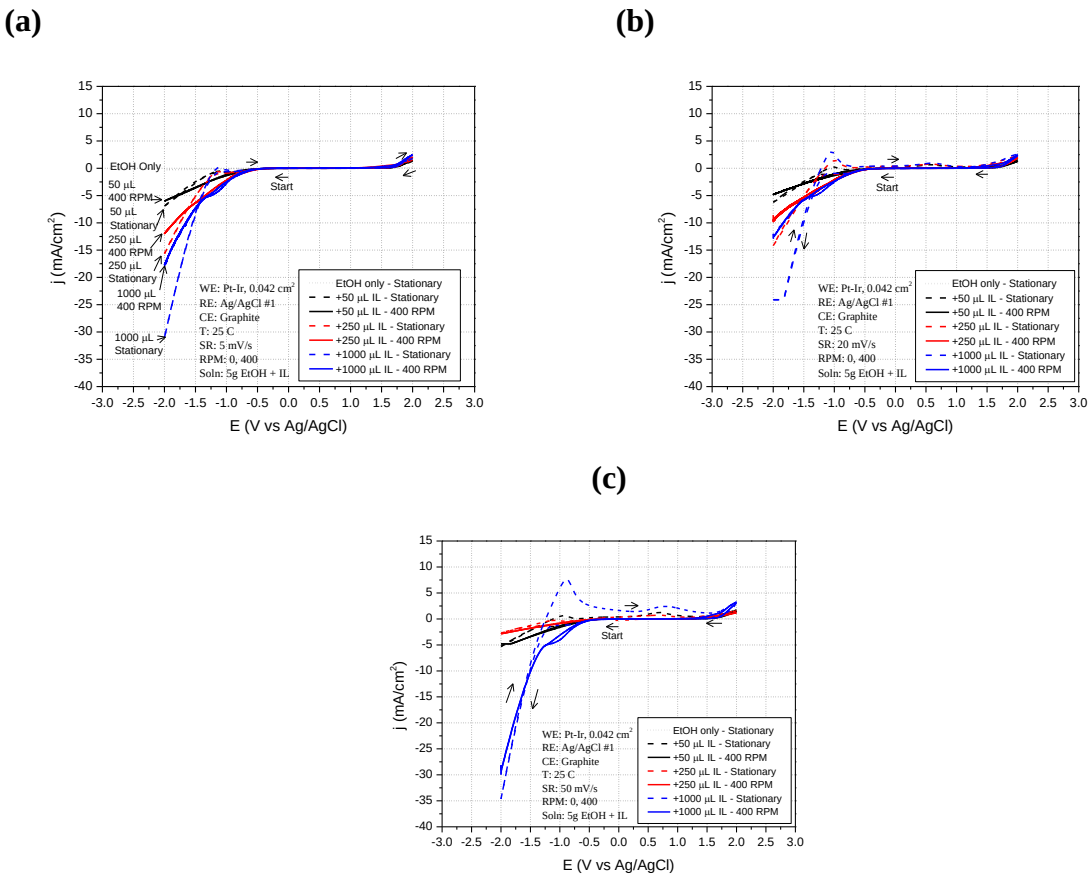

Figure 4.7: CV to examine the effects of incremental IL addition to a 5g sample of ethanol with no $NdCl_3$ present with 0 and 400 RPM rotation speeds**(a)** scan rate: 5 mV/s **(b)** scan rate: 10 mV/s **(c)** scan rate: 50 mV/s.

Figure 4.7a presents the cyclic voltammograms of an ethanol solution with incremental amounts of ionic liquid added. CV's were performed with a scan rate of 5 mV/s, with and without rotation at 400 RPM. Notice that initially, the experiments with 400 RPM present larger current densities than those performed at stationary conditions. This observation is consistent with the fundamental concept of the Levich equation, i.e. the shrinking boundary film drives faster mass transport and thus a larger reaction rate. However, once the applied potential reaches approximately -2 V for the 50µL addition scan, the scan at the stationary condition surpasses the scans with 400 RPM rotation and presents larger current densities. For the rest of the scan towards the cathodic direction, the stationary CV scan demonstrates larger current densities than the CV scan with 40 RPM. This transition from 400 RPM to stationary conditions providing the largest current densities requires careful

examination. An identical transition can be seen at -1.75 V for the 250μL IL addition, and -1.5 V for the 1000μL IL addition CV scans

This transition can be understood in light of the observations made by Schmidt et al. [37], who proposed the two step reduction process for ethanol discussed above and reproduced below in Equations 10 and 11.

$$CH_3CH_2OH + e \rightarrow CH_3CH_2OH^-_{adsorbed} \quad \text{Eqn. 10}$$

$$CH_3CH_2OH^-_{adsorbed} + e + 2H^+ \rightarrow CH_3CH_3 + H_2O \quad \text{Eqn. 11}$$

The first step in the reduction process was the adsorption of an ethanol radical followed by reduction to ethane gas. In light of the two step process just described for the reduction of ethanol on platinum, the experimental results seen in Figure 4.7a can be clarified. In experiments where no rotation speed was used. The adsorbed ethanol species remained on the surface longer and were fully converted to ethane or methane reduction products. However, when rotation was present, some of the adsorbed species were removed from the surface by the rotation. Removing the adsorbed species led to smaller currents during the rest of the scan as the remaining species were converted to ethane or methane.

This concept of the adsorbed intermediate species in the reduction process of ethanol can be further seen in the experimental results presented in Figures 4.7b and 4.7c with faster scan rates of 20 mV/s and 50 mV/s respectively. Notice that in both of these figures, when no rotation speed was used, an anodic peak was detected after the scan was reversed from the cathodic to anodic scan direction. These anodic currents are not seen when 400 RPM of rotation speed was used. These anodic currents are attributed to the oxidation of the adsorbed ethanol radicals that remained on the electrode surface. These anodic currents are not seen in the 400 RPM scans as the rotation of the electrode removes the species from the surface before they can be oxidized. These anodic currents were also not seen in Figure 4.7a in experiments with and without rotation as the slower scan rate of 5 mV/s used in Figure 4.7a allowed the adsorbed species to leave the surface before they could be oxidized. In all experiments seen in Figures 4.7a-c, it can be seen that the currents increase consistently with increasing additions of ionic liquid. This observation is explained by the ionic liquid providing greatly increased charge carrier concentrations to the ethanol solution.

4.8 Effect of IL addition to ethanol solutions with neodymium present

Previous experiments presented in Figures 4.7a-c discussed the incremental addition of ionic liquid to ethanol without neodymium present. To understand the reactions of ethanol when $NdCl_3$ is present, an identical batch of experiments was performed using a 5g ethanol solution with 125 mg of $NdCl_3$ added. Ionic liquid was then added incrementally and the results are shown in Figures 4.8c and 4.8d. Due to the large electronegative potential required for neodymium deposition (more cathodic than -2.5 V), the addition of neodymium chloride to ethanol/ionic liquid mixtures is not expected to produce any new peaks or behaviors within the voltage range studied. Experiments seen above in Figures 4.7a-c indicate that ethanol breakdown begins at approximately -1 V, well before any electrochemical reactions of neodymium are expected to occur.

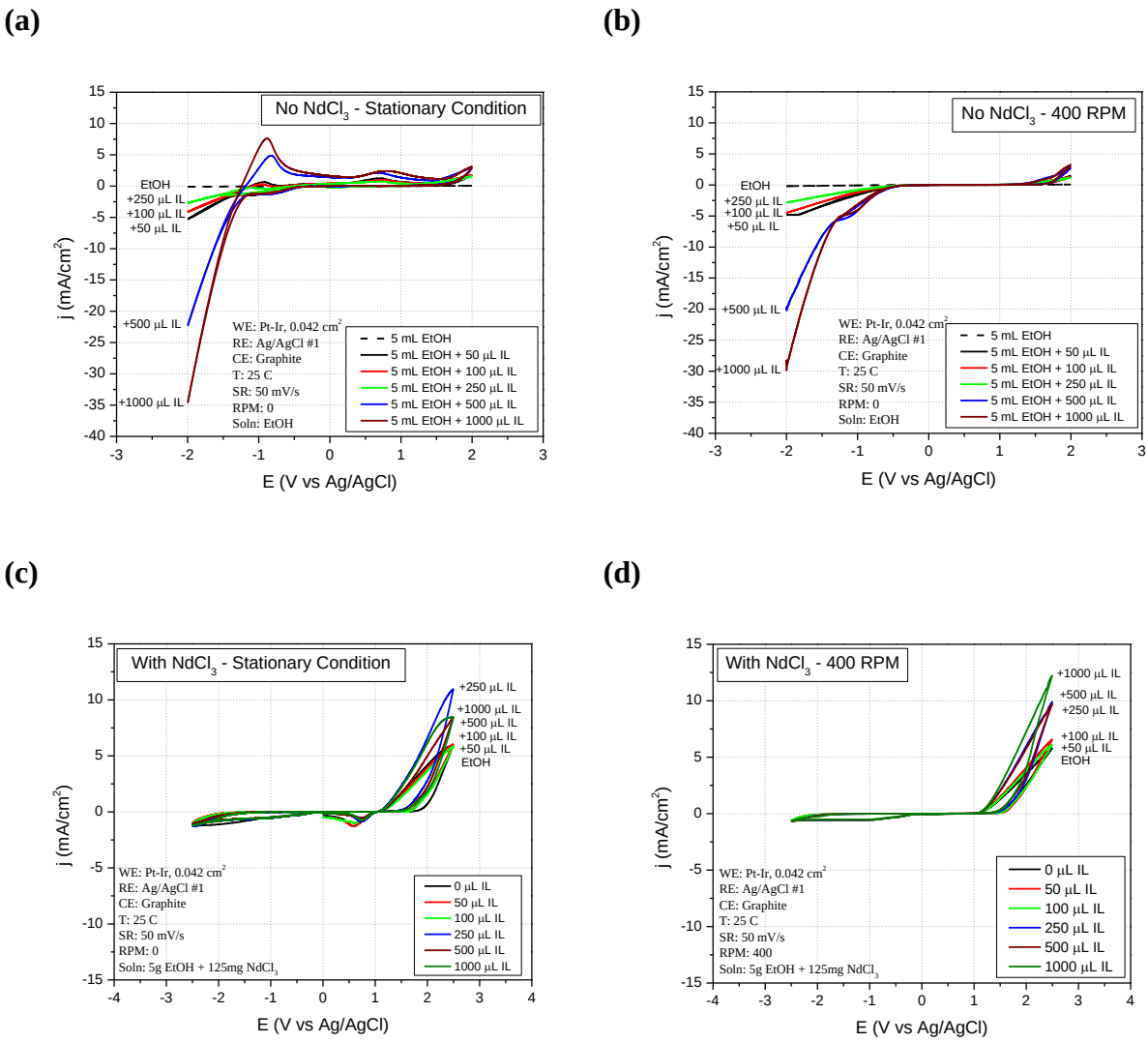

Figure 4.8: CV performed at 50 mV/s to examine the effects of incremental IL and $NdCl_3$ addition on the CV of EtOH **(a)** 0 RPM, no $NdCl_3$ **(b)** 400 RPM, no $NdCl_3$ **(c)** 0 RPM, with $NdCl_3$ **(d)** 400 RPM, with $NdCl_3$.

Figures 4.8a and 4.8b present the same data as Figure 4.7c above, with the 0 and 400 RPM experiments plotted on separate graphs. Notice again that the anodic currents disappear with rotation speed, indicating that an adsorbed reaction intermediary is being spun away from the electrode surface. A distinct change in the behavior in the plots is seen with the addition of $NdCl_3$ as seen in Figures 4.8c and 4.8d. The addition of $NdCl_3$ suppresses the

cathodic currents even with up to 1000μL of BMP-TFSI added to provide solution conductivity.

The first possible explanation for the suppression of the cathodic currents in Figure 4.8c and 4.8d is the deposition of a neodymium film achieved via a disproportionation reaction. For neodymium, the disproportion reaction first requires the single electron reduction of neodymium as seen below in Equation 13.

$$Nd^{3+} + e \rightarrow Nd^{2+} \qquad \text{Eqn. 13}$$

It is generally accepted that Nd^{2+} is unstable and will decay via a disproportionation reaction as presented in Equation 14 below.

$$3Nd^{2+} \rightarrow 2Nd^{3+} + Nd^{0} \qquad \text{Eqn. 14}$$

Chou and Hussey [19] observed a cathodic peak in the cyclic voltammograms in their RTIL occurring around the potential of -1.5 V vs a Ag/Ag+ reference electrode. They proposed that this peak should be attributed to reduction of Nd^{3+} to Nd^{2+} as seen in Equation 13. Once the neodymium film is deposited, the new neodymium surface would most likely have a smaller exchange current density for the reduction of ethanol compared to the original platinum surface. In order to confirm this assumption, Tafel polarizations were performed using both the bare platinum surface, as well as the platinum electrode with an electrochemically prepared neodymium surface. A Tafel polarization is a specific type of LSV experiment where the potentials scanned from -250mV to +250mV vs the equilibrium working electrode potential at a slow scan rate. The Tafel polarizations are presented below in Figure 4.9. Tafel polarizations provide quick and definitive values for the exchange current densities for the possible reactions occurring on the electrode surfaces. The Tafel polarizations were performed to determine if an electrodeposited neodymium film lead to lower exchange current densities for ethanol reduction.

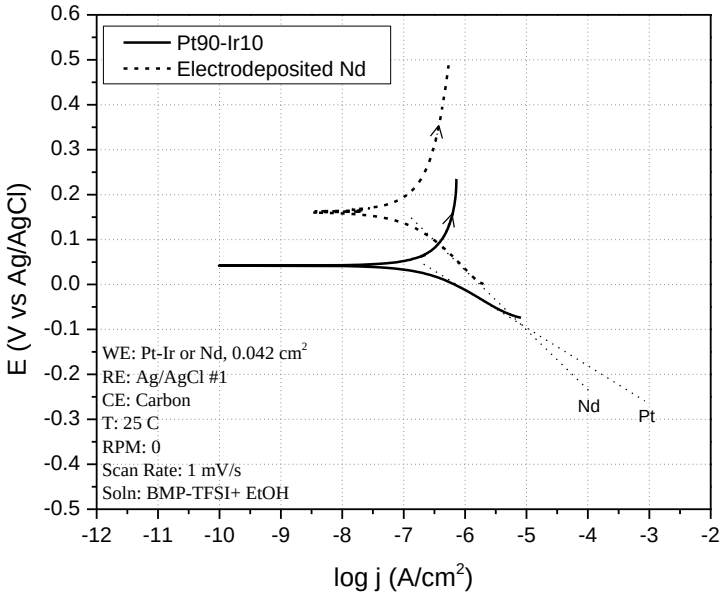

Figure 4.9: Tafel polarizations to examine effect of electrode surface chemistry on the redox reactions of ethanol. SR: 1 mV/s, T: 25 C.

The Tafel polarizations presented above in Figure 4.9 clearly illustrate that platinum will provide a larger exchange current density for the reduction of ethanol compared to an electrodeposited neodymium surface. The neodymium surface was prepared by cathodically polarizing the electrode in an ionic liquid with $NdCl_3$ present. Once the polarization was complete, the electrode was removed from the solution, while allowing a drop of ionic liquid to remain on the surface of the electrode, protecting the surface from the open atmosphere. The electrode was then immediately inserted into a new electrochemical cell containing ionic liquid with only ethanol added and the Tafel polarization begun.

By extrapolating the linear regions of the cathodic branch of the Tafel plots, the exchange current density for the reduction of ethanol on the two different surfaces can be predicted. Notice that the linear extrapolation of the electrodeposited neodymium film is significantly steeper than that of the polished platinum surface. This indicates that the exchange current density for ethanol reduction on neodymium will be significantly smaller compared to platinum. The Tafel polarizations confirm the theory that a neodymium film deposited by disproportionation could be the cause of smaller current densities for ethanol

when $NdCl_3$ is present. The rare earths are commonly known to act as catalysts, however, here neodymium deposition is seen to reduce the reduction current densities. Literature is scarce on the reduction reactions of ethanol. Schmidt [38] found that the redox reactions of ethanol proceeded rapidly on platinum, but no redox reactions were observed on a ruthenium electrode. It is possible that in this situation, neodymium metal behaves in a similar fashion as ruthenium, and electrodeposits of neodymium provide greatly reduced ethanol reduction current densities.

While it has been just shown that a neodymium film by disproportionation would lead to smaller ethanol reduction currents, it is unlikely that neodymium film formation is occurring in these experiments. Close examination of the scans presented in Figures 4.8c and 4.8d reveal no appreciable peaks attributable to the disproportion of neodymium. Note also that the suppression of the currents begins at approximately -1 V. This observation is particularly prominent in Figure 4.8d. Comparing this potential with the work of Hussey and Chou [19] discussed above reveals that the suppression of the anodic current begins roughly 500 mV before that which has been thermodynamic established for the first electron reduction of neodymium.

A second possibility for the suppression of the anodic currents could be the strong chemisorption of a $NdCl_3$-ethanol solvate. This stable solvate would resist electrochemical reduction, and its occupation of the surface would shield the electrode from free ethanol molecules. These two effects would lead to the markedly small currents seen in the cathodic region in Figures 4.8c-d. In order to determine if this phenomenon was occurring, experiments were performed in pure ethanol with 0.2 M $CaCl_2$ salt added to provide solution conductivity. After a baseline CV scan was performed in this solution, a second scan was performed with 0.1 M of neodymium chloride added. The results are presented below in Figure 4.10.

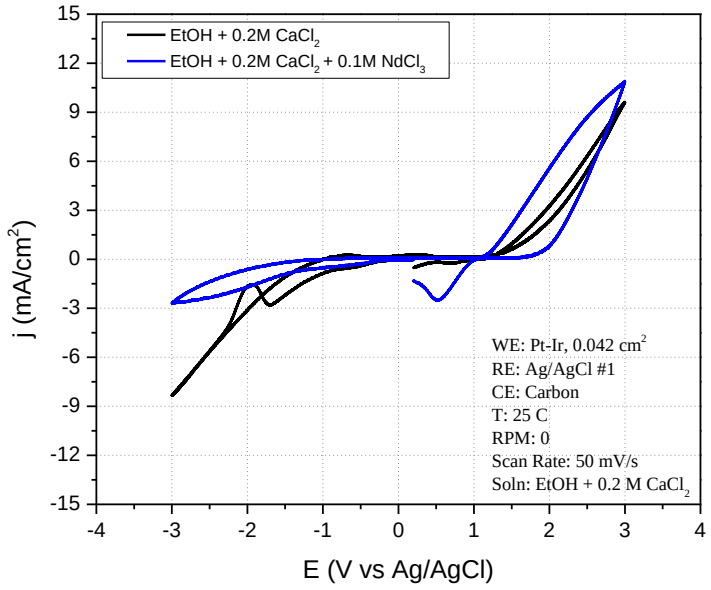

Figure 4.10: CV of ethanol with 0.2 M $CaCl_2$ added to examine the effect of 0.1M $NdCl_3$ addition.

Examining Figure 4.10 closely indicates that the addition of $NdCl_3$ to ethanol leads to large reductions in the cathodic currents. This is opposite of the expected increase in currents with the increased solution conductivity from the extra ions of $NdCl_3$. Comparing the current values of the scans in Figure 4.8c and 4.8d with those seen above in Figure 4.10 show that all the scans with $NdCl_3$ added are almost identical in terms of current densities. Meanwhile, the scan without $NdCl_3$ present presents significantly larger currents. The scans in Figure 4.10 indicate the formation of a strongly adsorbed $NdCl_3$-ethanol solvate that screens the working electrode surface from solution. This adsorbed solvate could also explain the results seen in Figures 4.8c-d. Solvation occurs when the solute atoms (in this case neodymium) are surrounded by concentric spheres of the solvent species (ethanol).

This proposed ethanol neodymium solvate fits well with the experimental data in Figures 4.8c and 4.8d. Without rotation in Figure 4.8c, the cathodic currents are all suppressed and present roughly the same value of roughly -1 mA/cm^2. In Figure 4.8d, with 400 RPM of rotation speed, the cathodic currents are still suppressed and with rotation all experiments virtually identical limiting current values of -0.6 mA/cm^2. This observation of

more consistent limiting currents with rotation can be explained by the rotation of the electrode creating a more uniform surface coverage of the strongly adsorbed solvate. This uniform surface coverage leads to very similar current density values for all experiments also explains the reduction in currents with rotation. The rotation helps promote a more uniformly adsorbed solvate layer which eliminates the few remaining sites on the electrode on which ethanol reduction can occur. Neodymium chloride-ethanol solvate complexes have been reported [45,46] with three molecules of ethanol assigned to each molecule of neodymium chloride.

4.9 CV of BMP-TFSI at low and high temperatures with and without $NdCl_3$

4.9.1 CV at 25° C and 100° C to examine the electrochemistry of BMP-TFSI without $NdCl_3$ present on Pt, Mo, and GC working electrodes

In order to understand the baseline stability of BMP-TFSI on platinum, molybdenum, and glassy carbon working electrodes, cyclic voltammetry was used to probe the electrochemical windows of the ionic liquid at 25° and 100° C. Platinum is well known for providing low required reaction overpotentials, combined with high exchange current densities. Glassy carbon on the other hand requires larger applied potentials for reactions to occur and due to its amorphous surface properties, provides small exchange current densities. Metallic molybdenum, while not as active as the platinum electrode should provide comparable required over potentials, while limiting the exchange current densities for undesirable ionic liquid breakdown.

(a) **(b)**

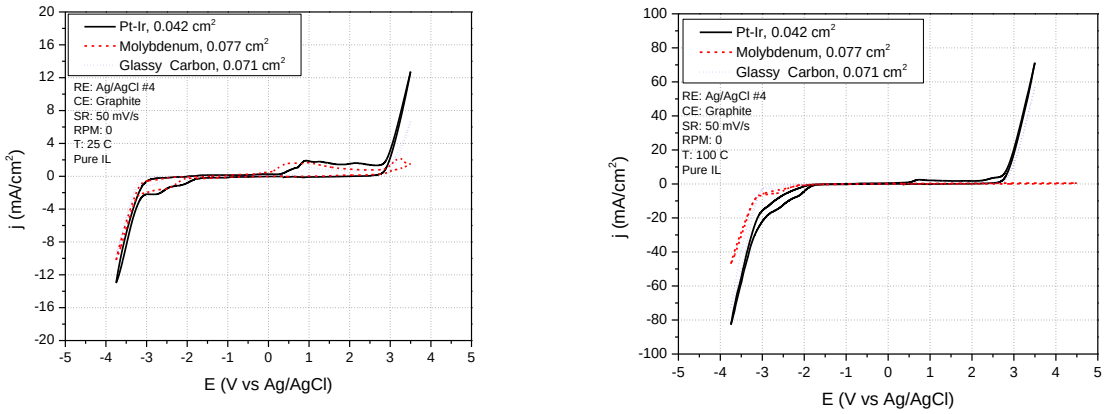

Figure 4.11: Baseline CV scans to study the electrochemistry of BMP-TFSI on Pt-Ir, Mo, and GC electrodes at room and high temperature **(a)** 25° C **(b)** 100° C.

Figure 4.11a shows that at 25° C the platinum and molybdenum working electrodes perform similarly in the cathodic region. In the cathodic region, glassy carbon performs the best out of the three electrodes in terms of increasing the stability range of BMP-TFSI. While all scans show severe breakdown of ionic liquid at approximately -3.2 V, glassy carbon provides the smallest current densities in the region from -2 to -3.2 V. In the anodic region the glassy carbon again presents the smallest current densities, while platinum and molybdenum present similar values. Notice however, that the molybdenum electrode does not present significant currents due to breakdown of the ionic liquid in the anodic direction. While breakdown in the cathodic direction should be attributed to reduction of the cation, breakdown in the anodic direction should be attributed to the oxidation of the anion. Based on this observation, it can be stated that the oxidation of the TFSI anion does not proceed rapidly on a molybdenum surface.

Figure 4.11b presents similar scans as Figure 4.11a with the temperature increased to 100 C. Again, the glassy carbon electrode performs the best in the cathodic region, as it presents the smallest current densities attributable to the reduction of the BMP cation. Molybdenum presents slightly larger currents than the glassy carbon, and the platinum surface provides the largest current densities. In the anodic direction, platinum again presents the

largest current densities and earliest break down. Glassy carbon presents smaller currents, while molybdenum again presents almost no anodic currents, even when scanned to +4.5 V. This observation again indicates that the oxidation of the TFSI anion does not proceed rapidly on the molybdenum surface.

The cathodic region and breakdown behavior of BMP-TFSI is of more importance than the anodic behavior as reduction of neodymium will occur in the cathodic region. Kroon et al. [47] used computational methods to simulate the cathodic breakdown products of the BMP cation. The computational results were corroborated with experiments and characterization with gas chromatography and mass spectroscopy. Kroon's computation results yielded three possible products for the breakdown of BMP. The first and most likely outcome is the creation of methylpyrrolidine and a butyl radical group. The second most likely is the splitting of the pyrrolidine ring and the formation dibutylmethylamine radical. The final and least likely outcome is the formation of butylpyrrolidine and a methyl radical.

4.9.2 CV at 25° C and 100° C to examine the electrochemistry of BMP-TFSI with $NdCl_3$ present on Pt, Mo, and GC working electrodes

With the baseline behavior of BMP-TFSI on platinum, molybdenum, and glassy carbon established in Figures 4.11a and 4.11b, neodymium chloride was added to the ionic liquid to examine the electrochemistry of neodymium in BMP-TFSI. CV scans of the ionic liquid-$NdCl_3$ solution are presented below in Figures 4.12a and 4.12b on platinum, molybdenum, and glassy carbon working electrodes at 25 and 100° C.

(a) **(b)**

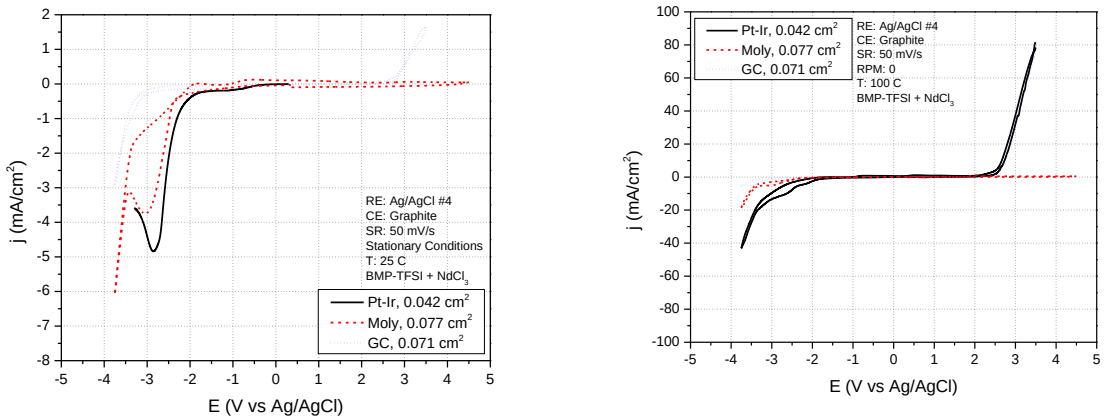

Figure 4.12: CV of BMP-TFSI on the Pt-Ir, Mo, and GC working electrodes in pure IL dried overnight with Nd present via HTFSI addition **(a)** 25° C **(b)** 100° C.

The CV scans shown above in Figure 4.12a present distinct peaks for Nd reduction beginning at approximately -2.75 V for platinum and ranging to -3 V for glassy carbon. As discussed above it is well known that the glassy carbon surface will require large over potentials compared to the platinum and molybdenum substrates. These peaks are not visible in the scans presented in Figure 4.12b when the temperature was increased to 100° C. The observation can be understood by the temperature induced instability of the BMP cation. The currents observed for Nd reduction in Figure 4.12a range from -3 to -5 mA/cm^2. Examining Figure 4.12b closely indicates that currents of this magnitude would be "drowned out" by the increased electrochemical degradation of the ionic liquid. Further efforts to study the cathodic peaks seen in Figure 4.12a will be made using LSV scans.

4.10 LSV of BMP-TFSI with Nd added on Pt, Mo, and GC working electrodes

The CV scans presented above in Figure 4.12a present distinct cathodic peaks that correspond well with the standard potential for neodymium reduction. These peaks are not present in the CV scans presented in Figure 4.11a at room temperature without neodymium present. To further study the peaks seen during the cathodic scans at room temperature discussed above in Figure 4.12a, linear sweep voltammetry was performed with the three

different electrodes. Linear sweep voltammetry was chosen instead of cyclic voltammetry in order to accurately study the deposits on the electrode surface directly after the peaks seen in the CV's. Because the CV's are scanned into the anodic direction after reaching the cathodic vertex potential, the surface deposits could be oxidized away or significantly altered by the anodic applied potentials. LSV scans for the Pt-Ir, Mo, and GC electrodes are presented below in Figure 4.13.

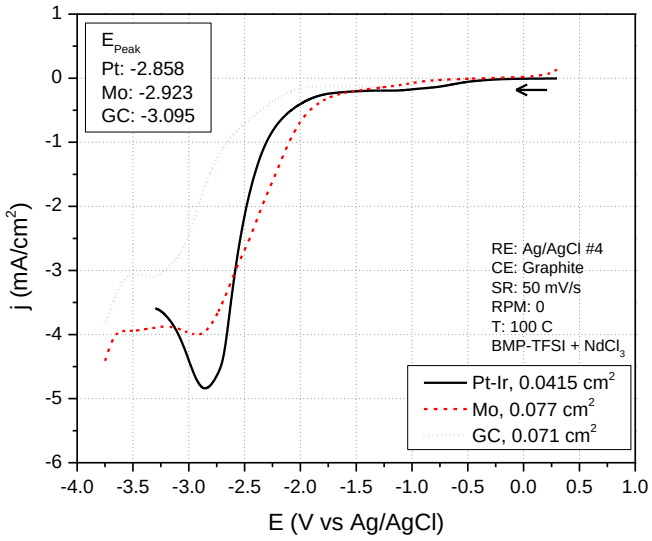

Figure 4.13: LSV scans of Pt-Ir, Mo, and GC working electrodes in BMP-TFSI with $NdCl_3$ added. Scans begun at +0.3 V. SR: 50 mV/s, T: 25° C.

The LSV scans presented in Figure 4.13 present distinct peaks in the cathodic region that correspond relatively well with the values reported for the standard potentials required for neodymium reduction. The platinum electrode presents the most well defined peak with the largest current density. This is consistent with known behavior of platinum for large exchange current densities and lower over potentials compared to other substrates. The molybdenum electrode presents the next largest current densities with the peak potential shifted approximately 70 mV in the cathodic direction compared the peak potential of the platinum electrode. Finally, the glassy carbon electrode presents the smallest peak current

densities and the most cathodic peak potential. It is generally known that glassy carbon requires larger over potential for deposition of metals compared to metallic electrodes like molybdenum and carbon. Notice in Figure 4.13 that there are no distinct peaks to be assigned to the single electron reduction of Nd^{3+} to Nd^{2+}. This observation is in contrast with the work of Chou and Hussey [19] who all showed a single electron reduction step for neodymium. Examining the thermodynamics of Nd in aqueous solution indicates that the reduction of Nd^{3+} to metallic Nd (-2.545 V) should occur before the single electron reduction of Nd^{3+} to Nd^{2+} at a potential of -2.85 V.

Immediately following the LSV experiments just discussed, the electrodes were imaged using optical microscopy to study the effect of surface on the films formed on each electrode. The following procedure was used to clean each electrode following the electrochemical experiments in ionic liquid. First, the residual ionic liquid around the electrode sleeve was removed with a Kimwipe, taking care to not touch the surface. Next the electrode was placed into two sequential methanol baths to remove any residual ionic from the surface. The electrode was placed in each methanol solution for approximately 5 minutes. After the second methanol bath, the electrode cleaned with a methylene chloride solution as a final cleaning step to remove any residual contaminants. Optical micrographs of the three working electrodes are presented below in Figures 4.14a-c

(a) **(b)** **(c)**

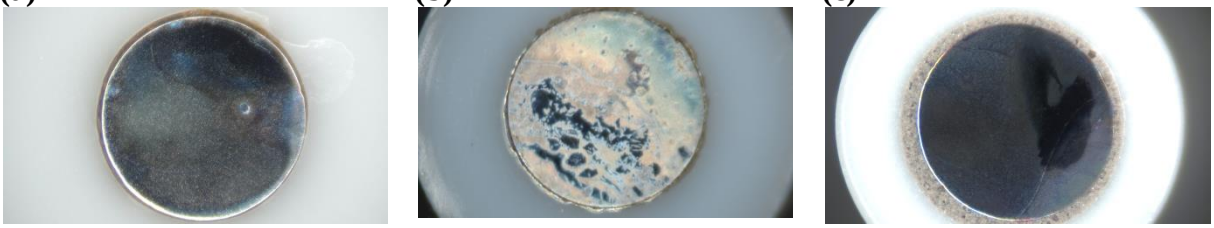

Figure 4.14: Optical micrographs taken at 40x magnification of working electrodes after LSV experiments **(a)** Pt-Ir **(b)** Mo **(c)** GC.

The optical micrographs presented above demonstrate that platinum and molybdenum provide the best film coverage, while glassy carbon provides slightly less surface coverage. This is consistent with the magnitudes of the peak current densities seen in the LSV scans in

Figure 4.13. These scans showed platinum and molybdenum to have the largest current densities compared to glassy carbon. As stated above, molybdenum provided much smaller currents for the breakdown of ionic liquid and provided comparable peak current densities for neodymium deposition compared to platinum. For these reasons, combined with the distinct film seen in Figure 4.14b, molybdenum again distinguishes itself as suitable electrode for neodymium deposition.

Based on the LSV scans and optical microscopy, it is apparent that either the molybdenum or platinum substrate will provide the best results for deposition of metallic neodymium from ionic liquids. While platinum presents the largest leak current densities for the deposition of neodymium, molybdenum performed better than platinum without neodymium present by delaying the onset of ionic liquid breakdown and allowing smaller current densities for the ionic liquid decomposition.

Chapter 5: Surface Morphology and Characterization

5.1 Optical characterization of electrodeposited films on a Pt working electrode at 25° C

Optical microscopy allows quick and easy verification that a film has been deposited. Figures 5.1a-g below present the effect of applied potential on the surface films formed on the platinum working electrode following potentiostatic polarization for 3 seconds. After each experiment the electrode was dipped in two successive methanol baths to remove excess ionic liquid. Directly before optical microscopy, the surface was cleaned with methylene chloride organic solvent to remove any residue.

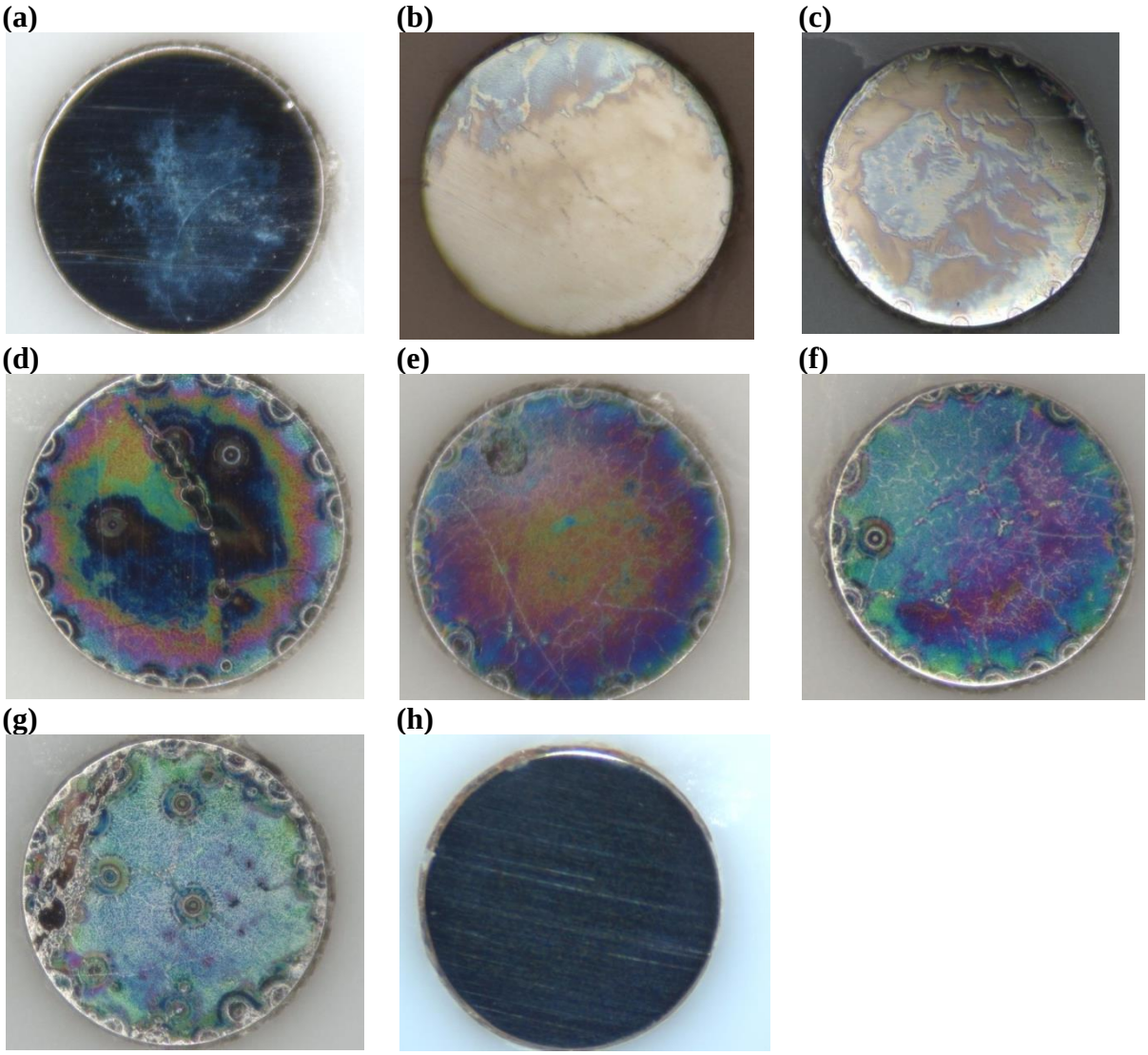

Figure 5.1: Film formation as a function of applied potential as characterized by optical microscopy. Films formed by CA performed for three seconds at 25° C with potentials of**(a)** -2.2 V **(b)** -2.4 V **(c)** -2.6 V **(d)** -2.8 V **(e)** -3 V **(f)** -3.2 V **(g)** -3.4 V **(h)** control sample polarized at -3 V for 3 seconds in pure IL with noNd present. All micrographs taken at 40 x magnification.

Figure 5.1a-g presents optical micrographs captured at 40x magnification for all images. Figure 5.1a was polarized at -2.2 V for 3 seconds and no substantial film is seen on the surface. In Figures 5.1b and 5.1c a distinct film is seen on the electrode surface with polarization potentials of -2.4 and -2.6 V respectively. These potentials correspond well with the onset of neodymium deposition beginning to occur at -2.5 V. With a larger over potential of -2.8 V, a more distinct film is observed on the electrode surface as seen in Figure 5.1d.

Notice also in this figure the circular areas present mainly around the edge of the electrode. These areas are attributed to the formation of bubbles on the electrode surface during polarization. The bubbles are explained by the presence of dissolved ethanol in the system as ethanol was used as an intermediate in the solution preparation process. The bubbling could also be produced from the electrolysis of water absorbed from the open atmosphere. Both of the reduction products of water and ethanol are gaseous species. As discussed above, ethanol is proposed to follow a two-step reduction process to methane or ethane, and hydrogen gas produced from water will also create bubbles on the surface. During CV experiments, bubbles were frequently observed on the electrode surfaces which were easily removed by tapping the electrode. These bubbles will obscure the surface area underneath and lead to an inconsistent film. Continued increase in applied over potential leads to complete coverage of the electrode surface with a polarization of -3 V as shown in Figure 5.1e, but again evidence of bubbling is present on the electrode surface. Polarization at -3.2 V and -3.4 V in Figures 5.1f and 5.1g leads to further increased bubbling on the electrode surface, disrupting neodymium layer formation. Figure 5.1h presents the electrode surface after polarization at -3 V for 3 seconds in a pure ionic liquid solution with no neodymium present. The bare surface evident in Figure 5.1h indicates that even up to -3 V, the deposits seen in Figure 5.1b-g should be attributed to the reduction of neodymium. This observation is critical as one considered explanation for the films seen was the deposition of the BMP cation from ionic liquid. The lack of deposits in Figure 5.1h indicates that the deposits must be attributed to neodymium related deposition rather than simple reduction and deposition of the BMP cation. A possible explanation for these films in the deposition of a neodymium chloride-ethanol solvate as discussed earlier. To rule out this possibility, one of the films shown above was dissolved in purified nitric acid. This acid was then added to a vial of nitric acid to check for the formation of solid silver chloride precipitates. No considerable formation of silver chloride was seen during these tests which indicates that chloride is not present in considerable amounts in the films deposited in Figures 5.1a-h.

5.2 SEM characterization of electrodeposited films on Pt, Mo, and GC working electrodes following LSV scans at 25° C

Immediately following the LSV scan shown in Figure 4.13, the platinum working electrode was cleaned in two successive methanol baths for at least five minutes each. The electrode was then cleaned using methylene chloride. Optical microscopy was first performed, followed by characterization using SEM. SEM micrographs of the Pt electrode surface are presented below in Figures 5.2a-c.

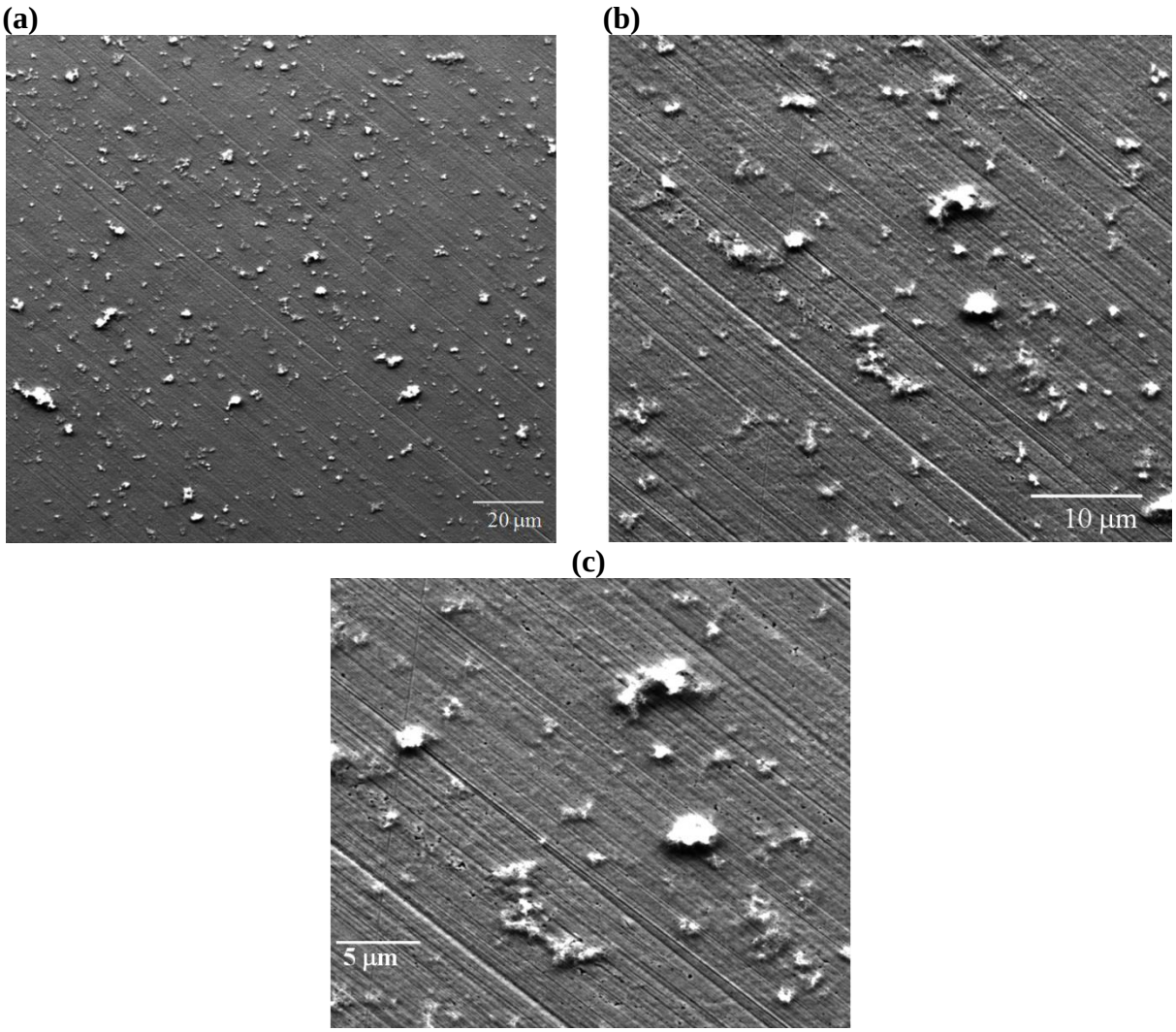

Figure 5.2: SEM characterization of the Pt working electrode after LSV in BMP-TFSI with $NdCl_3$ present at 25° C **(a)** 1,000x magnification **(b)** 3,000x magnification **(c)** 5,000x magnification.

Figures 5.2a-c above present SEM images of the platinum working electrode surface following linear sweep voltammetry in the cathodic region. In all three images above, the presence of white clumps is noted that appear to be charging under the SEM. These clumps are attributed to agglomeration of ionic liquid breakdown product. It should be noted that this breakdown product is very stable as soaking in methanol for at least 10 minutes and rinsing with methylene chloride did not completely remove the deposits. Of importance to note are the micro scale porosities seen in the film present. These porosities are particularly evident in Figure 5.2c. These porosities are attributed to the evolution of a gaseous product on the electrode surface. In this case these gaseous species are likely the generation of hydrogen gas from moisture that the ionic liquid absorbed from the atmosphere. It is unlikely that any breakdown products of the ionic liquid as discussed earlier would lead to the formation of gaseous products. Figures 5.2a and 5.2b indicate that the deposited film uniformly covers the entire platinum surface.

In a similar fashion as the platinum electrode just discussed, SEM characterization was performed on the glassy carbon and molybdenum electrodes following LSV scans in BMP-TFSI with $NdCl_3$ present. The results are presented below in Figures 5.3a and 5.3b.

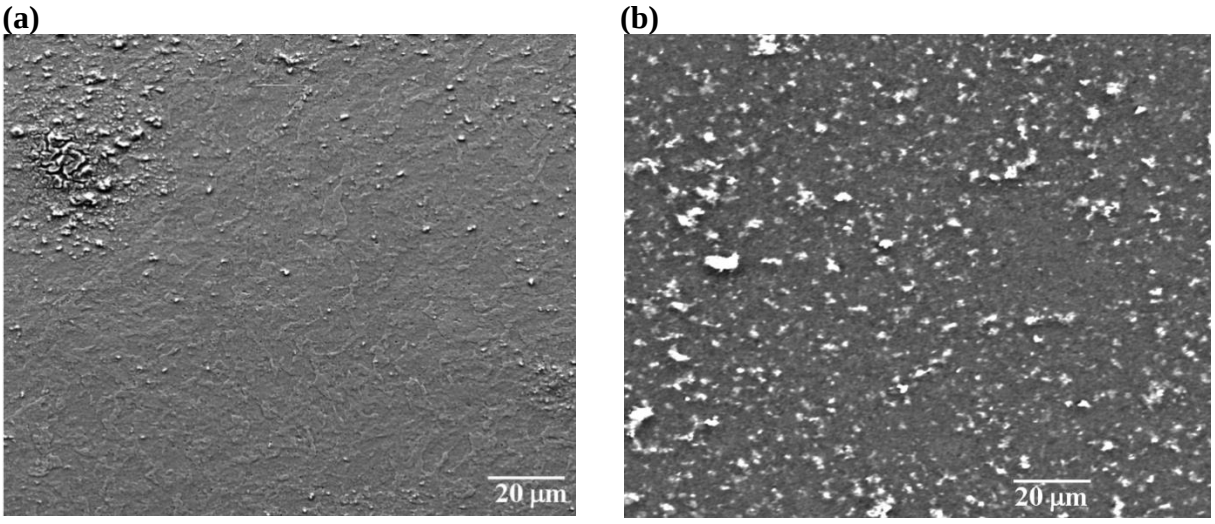

Figure 5.3: SEM characterization at 1,000x magnification of electrode surfaces after LSV to -3.5 V in BMP-TFSI with $NdCl_3$ present at 25° C **(a)** Molybdenum electrode **(b)** Glassy carbon electrode.

The electron micrograph of the film deposited on the molybdenum electrode provides almost total coverage. The film is also very dense, as the electrode surface cannot be seen in Figure 5.3a. However, it should be noted that there are thousands of tiny pores present which are evident of a gaseous product during the deposition process. This observation agrees well the film seen on the platinum working electrode. This gaseous product could be the electro-generation of hydrogen gas from moisture adsorbed into ionic liquid from the open atmosphere. EDX imaging of the surfaces is planned to characterize the chemical composition of the films. There are also cracks present in the films seen on the molybdenum electrode (seen as lighter lines). It is proposed that these cracks arise from the preferential generation of hydrogen gas at the electrode's grain boundaries. These bubbles eventually crack the film as they escape. No such cracks are observed on the glassy carbon electrode, as should be expected due to the amorphous nature of glassy carbon. The white residue present particularly on the glassy carbon electrode is again proposed to be a breakdown product of the ionic liquid. This breakdown product is very difficult to remove as mentioned above. Even prolonged soaking in methanol followed by air blow drying was unable to remove it.

5.3 SEM characterization of electrodeposited film on a Pt working electrodes following potentiostatic deposition at 100° C

To study the film morphology at higher temperature, experiments were performed using the heated cell setup shown in Figure 3.8b. Figure 5.4a-d below present electron micrographs of the platinum working electrode after CA performed in BMP-TFSI with $NdCl_3$. This electrode was polarized at -3.5 V for 3 hours with the temperature increased to 100° C. The increased temperature could encourage film formation by weakening the adsorption of BMP cations on the working electrode surface. With the extra thermal energy supplied, the cations would be forced off the surface, which would leave openings for metal deposition.

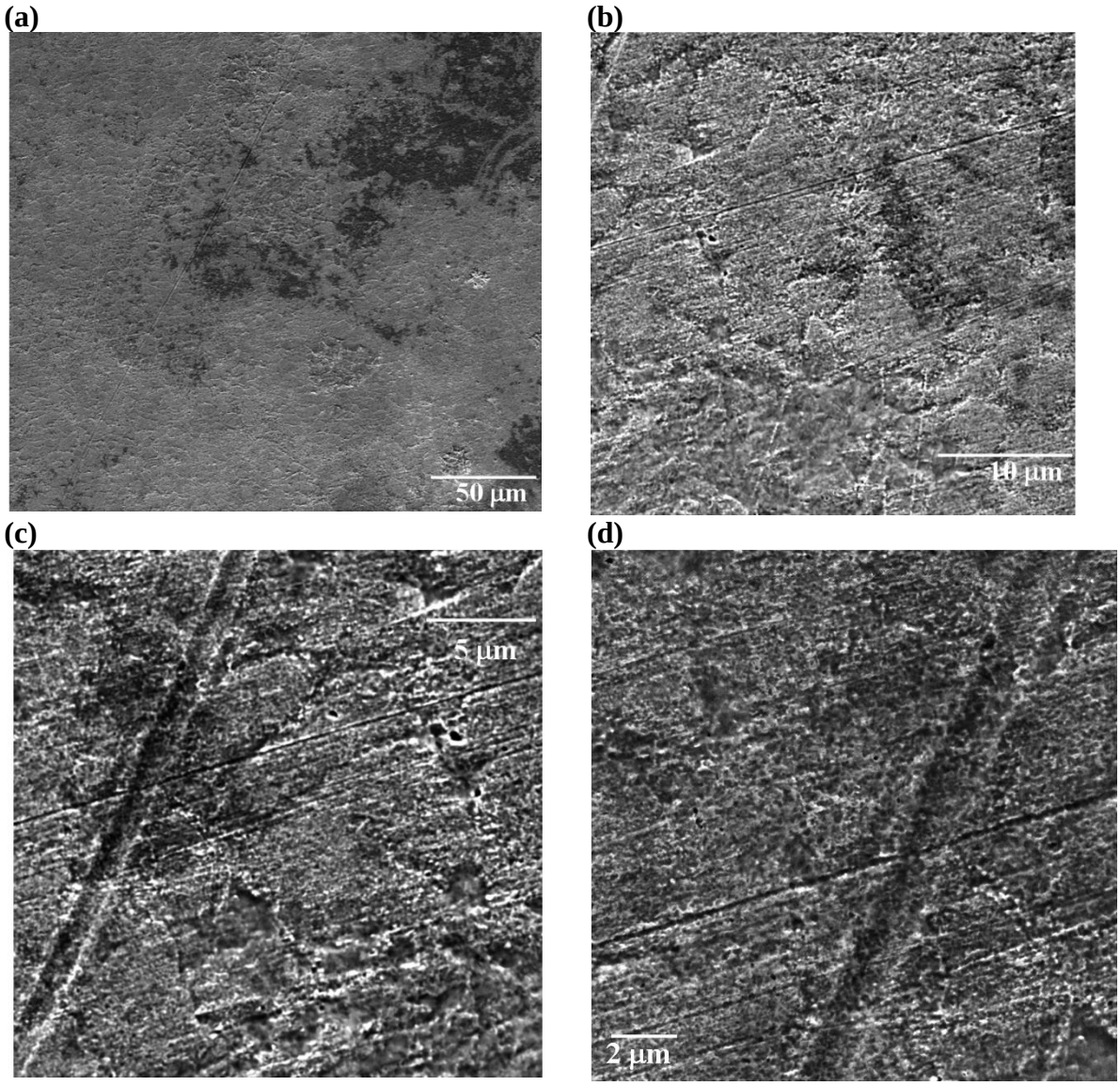

Figure 5.4: SEM characterization of electrodeposit morphology on the platinum working electrode. Potentistatic deposition performed for 3 hours at -3.5V at 100 C. **(a)** 600x **(b)** 4,000x **(c)** 6,000x **(d)** 10,000x.

Notice in Figures 5.4a-d that there appear to be two separate films deposited on the surface of the electrode, one on top of the other. The lighter film covers almost the entire electrode surface, while only patches of the darker layer are visible underneath. Examining Figure 5.4d indicates that the darker layer is also a film on the electrode surface and not the bare electrode surface itself. Even in the darker patches on either side of the scratch, a rough surface is seen which is not the well polished electrode surface. Also in Figure 5.4d, notice

the many tightly clustered spheres that line the deeper scratch. These spheres are consistent with metallic nucleation which is drawn to scratches on the electrode surface. Scratches on an electrode surface are well known to provide the highest energy density, and thus nucleation occurs first along the scratches.

Chapter 6: Potential for Further Research

To continue this research, I would recommend careful characterization of the chemical composition of the films deposited on the working electrodes after both potentiodynamic and potentiostatic experiments. X-ray diffraction (XRD) would provide the most conclusive results for this type of work. Energy dispersive X-ray (EDX) analysis could also provide valuable information on the chemical composition; however, EDX cannot distinguish between a metallic neodymium deposit and a neodymium chloride–ethanol-ionic liquid compound that could have been electrodeposited on the electrode surface. XRD on the other hand would be far more selective in its characterization. Because of the small sample size and the thin films deposited on the electrodes, a specialized XRD machine would be required for the glancing angle thin film characterization. It is likely that once exposed to open atmosphere, the neodymium films rapidly oxidize to form a protective oxide layer that could be detected using XRD. If EDX must be used, particular attention should be payed to presence of chlorine in the spectra. If no chlorine is present, it is likely that the film is metallic or metal oxide.

Following EDX or XRD experiments, more specific potentiostatic (CA) studies should be performed. It has been shown in this work with optical microscopy that films are clearly deposited from BMP-TFSI with $NdCl_3$ but not without neodymium present. In order to examine the metallic nucleation mechanisms of neodymium from BMP-TFSI, potentiostatic deposition experiments should be run around the peak potentials seen in the LSV scans in Figure 30. The CA experiments could then be modelled with the Sharifker-Hills nucleation equations to demine if neodymium deposits via the instantaneous or progressive nucleation mechanism. SEM characterization of the nuclei size as a function of time would confirm the nucleation mechanism. Once a baseline is established, the effects of temperature should be studied to determine if these parameters influence the nucleation mechanism. The effect of electrode surfaces in platinum, molybdenum, and glassy carbon should also be studied to analyze their influences on the deposition mechanism and film morphology.

Chapter 7: Summary and Conclusions

Based on the electrochemical experiments presented in this work, the following conclusions have been made.

1. The Ag/AgCl reference electrode used in these experiments provides a stable and reproducible reference potential for further use. The effectiveness (stability) of the electrode was evaluated with respect to the redox reactions of hydrogen and ferrocene in BMP-TFSI.
2. Water and ethanol both drastically reduce the electrochemical window of BMP-TFSI from approximately 6 volts to 2 volts. The diffusion coefficients of water and ethanol were evaluated to be 7.6×10^{-7} cm^2/sec and 1.8×10^{-9} cm^2/sec respectively. The reduction of ethanol on platinum in BMP-TFSI exhibited sluggish kinetics and the rate constant was calculated to be 4.3×10^{-4} cm/sec.
3. Based on CA and optical microscopy, Nd deposition on platinum from BMP-TFSI begins between -2.2 V and -2.4 V vs the Ag/AgCl reference. Larger over potentials lead to thicker surface coverage but also to gaseous product generation on the electrode surface.
4. LSV experiments indicate no single electron transfer step from Nd^{3+} to Nd^{2+} is evident in these experiments. A single cathodic peak is evident on Pt, Mo, and GC working electrodes beginning at approximately -2.75 V which is consistent with the required overpotential for Nd deposition from trivalent neodymium.
5. The molybdenum electrode provides the best overall electrochemical properties for further study of metal behavior in BMP-TFSI. It exhibits smaller currents and delayed onset for ionic liquid breakdown, while still providing Nd deposition only 70 mV more cathodic than platinum.
6. SEM characterization indicated the formation of a two layered film on the electrode surface. The layer closest to the electrode surface was observed to have micro-porosities present which indicate the generation of a gaseous product. On top of this porous layer, a second layer was observed attributed to deposition of reaction product from the breakdown of the ionic liquid.

References

[1] Weast, R., Astle, M. & Beyer, W., CRC handbook of chemistry and physics: a ready-reference book of chemical and physical data, Boca Raton, Fla: CRC Press (1985).

[2] Kim, G-Y., Yoon, D., Paek, S., Kim, S-H., Kim, T-J., Ahn, D-H., A study on the electrochemical deposition behavior of uranium ion in a LiCl–KCl molten salt on solid and liquid electrode, Journal of Electroanalytical Chemistry 682 (2012) 128-135.

[3] Liu, Ya-Lan, Yuan, Li-Yong, Kui-Liu, Ye, Guo-An, Zhang, Mi-Lin, He, Hui, Tang, Hong-Bin, Lin, Ru-Shan, Chai, Zhi-Fang, & Shi, Wei-Qun, Electrochemical extraction of samarium from LiCl-KCl melt by forming Sm-Zn alloys, Electrochimica Acta 120 (2014) 369-378.

[4] Rappleye, D., & Simpson, M. F., Application of the rotating cylinder electrode in molten LiCl-KCl eutectic containing uranium(III)- and magnesium(II)-chloride. Journal of Nuclear Materials 487 (2017) 362-372.

[5] Basin, A.S., Kaplun, A.B., Meshalkin, A.B., Uvarov, N.F., The LiCL-KCl binary system, Russian Journal of Inorganic Chemistry 53 (2008) 9:1509-1511.

[6] Lee, J-H., Kang, Y-H., Hwang, S-C., Shim, J-B., Ahn, B-G., Kim, E-H., Park, S-W., Electrodeposition Characteristics of Uranium in Molten LiCl–KCl Eutectic and its Salt Distillation Behavior, Journal of NUCLEAR SCIENCE and TECHNOLOGY,43 (2006) 3: 263–269.

[7] Walden, H., Bulletin de L'AcademieImperiale des Scieces de St. Petersburg, 8 (1914) 405-422.

[8] Wilkes, J.W., Levisky, J.A., Wilson, R.A., Hussey, C.L., Diaklylimidazolium chloroaluminate melts: A new class of room-temperature ionic liquids for electrochemistry, spectroscopy, and synthesis, Inorganic Chemistry 21 (1982) 3: 1263-1264.

[9] Park, J., Jung., Y., Kusumah, P., Lee, J., Kwon, K., Lee, C.K., Application of ionic liquids in hydrometallurgy, International Journal of Molecular Sciences 15 (2014) 15320-15343.

[10] Hajipour, A.R., Rafiee, F., Basic ionic liquids. A short review, Journal of the Iranian Chemical Society 6 (2009) 4:647-678.

[11] Nakashima, K., Kubota, F., Maruyama, T., Goto, M., Ionic liquids as a novel solvent for lanthanide extraction, Analytical Sciences 19 (2003) 1097-1098.

[12]Mudring, A., Tang, S., Ionic liquids for lanthanide and actinide chemistry, European Journal of Inorganic Chemistry (2010) 2569-2581.

[13] Zhang, Q.B., Yang, C., Hua, Y.X., Li, Y., Dong, P., Electrochemical preparation of nanostructured lanthanum using lanthanum chloride asa precursor in 1-butyl-3-methylimidazolium dicyanamide ionic liquid, Physical Chemistry Chemical Physics 17 (2015) 4701-4707.

[14] Nikitenko, S.I., Cannes, C., Le Naour, C., Moisy, P., Trubert, D., Spectroscopic and electrochemical studies of U(IV)-hexachloro complexes in hydrophobic room-temperature ionic liquids, Inorganic Chemistry 44 (2005) 6497-9505.

[15] Bhatt, A.I., Duffy, N.W., Collison, D., May, I., Lewin, R., Cyclic voltammetry of Th(IV) in the room-temperature ionic liquid $[Me_3N^nBu][N(SO_2CF_3)_2]$, Inorganic Chemistry 45 (2006) 1677-1682.

[16] Legeai, S., Diliberto, S., Stein, N., Boulanger, C., Estager, J., Papaiconomou, N., Draye, M., Room-temperature ionic liquid for lanthanum electrodeposition, Electrochemistry Communications 10 (2008) 1661-1664.

[17] Matsumiya, M., Kikuchi, Y., Yamada, T., Kawakami, S., Extraction of rare earth ion by tri-n-butylphosphate/phosphonium ionic liquids and the feasibility of recovery by direct electrodeposition, Separation and Purification Technology 130 (2014) 91-101.

[18]Matsumiya, M., Ishi, M., Kazama, R., Kawakami, S., Electrochemical analyses of diffusion behaviour and nucleation mechanisms for neodymium complexes in [DEME][TFSA] ionic liquid, Electrochimica Acta 146 (2014) 371-377.

[19] Chou, L., Hussey, C., An electrochemical and spectroscopic study of Nd(III) and Pr(III) coordination in the 1-butyl-1-methylpyrrolidinium bis(trifluoromethylsulfonyl)imide ionic liquid containing chloride ion, Inorganic Chemistry 53 (2014) 5750-5758.

[20] Pan, Y., Hussey, C., Electrochemical and spectroscopic investigation of Ln3+ (Ln = Sm, Eu, and Yb) salvation in bis(trifluoromethylsulfonyl)imide-based ionic liquids and coordination by N,N,N',N'-Tetraoctyl-3-oxa-pentane diamide (TODGA) and chloride, Inorganic Chemistry 52 (2013) 3241-3252.

[21] Roa C.J., Venkatesan, K.A., Nagarajan, K., Srinivasan, T.G., Vasudeva, P.R., Electrochemical behaviour of europium (III) in N-butyl-N-methylpyrrolidiniumbis(trifluoromethylsulfonyl)imide, Electrochimica Acta 54 (2009) 4718-4725.

[22] Yang, X., He, L., Qin, S., Tao, G-H., Huang, M., Lv, Y., Electrochemical and thermodynamic properties of Ln(III) (Ln = Eu, Sm, Dy, Nd) in 1-butyl-3-methylimidazolium bromide ionic liquid, PLoS One 9 (2014) 4:e95832.

[23] Gosser, D.K., Cyclic Voltammetry: simulation and analysis of reaction mechanisms, VCH Publishers, New York, New York (1993).

[24] Mirceski, V., Gulaboski, R., Lovric, M., Bogeski, I., Kappl, R., Hoth, M., Square-Wave Voltammetry: A review of the recent progess, Electroanalysis 25 (2013) 11:2411-2422.

[25] Nikolic J.; Exposito, E.; Iniesta, J.; Gonzalez-Garcia, J.; Montiel, V., Theoretical Concepts and Applications of a Rotating Disk Electrode, Journal of Chemical Education 77 (2000) 9:1191-1194.

[26] Bard, A.J., Faulkner, L.A., Electrochemical Methods: Fundamentals and Application, John Wiley and Sons, New York, New York (1980).

[27] Pesic, B., Advanced Electrochemical Separations of Actinide/Fission Products via the Control of Nucleation and Growth of Electrodeposits, U.S. Department of Energy, DOE-NEUP Award Number DE-NE00008556 (2016).

[28] Bentley, C.L., Bond, A.M., Hollenkamp, A.F., Mahon, P.J., Zhang, J., Mass transport studies and hydrogen evolution at a platinum electrode using bis(trifluoromethylsulfonyl)imide as the proton source in ionic liquids and conventional solvents. Journal of Physical Chemistry C 118 (2014) 29663-29673.

[29] Meng, Y., Aldous, L., Belding, S.R., Compton, R.G., The hydrogen evolution reaction in a room temperature ionic liquid: mechanism and electrocatalyst trends, Physical Chemistry Chemical Physics 14 (2012) 5222-5228.

[30] Gagne, R.R., Koval, C.A., Lisensky, G.C., Ferrocene as an internal standard for electrochemical measurements, Inorganic Chemistry 19 (1980) 9:2854-2855.

[31] Torriero, A.A.J., Howlett, P.C., Ionic liquid effects on the redox potential of ferrocene, Electrochemistry Communications 16 (2012) 84-87.

[32] O'Toole, S., Pentlavalli, S., Doherty, A.P., Behavior of electrogenerated bases in room-temperature ionic liquids. Journal of Physical Chemistry B 11 (2007) 9281-9287.

[33] Tang, Y., Lin, L., Kumar, A., Guo, M., Sevilla, M., Zeng, X., Hydrodgen electrooxidation in ionic liquids catalyzed by the NTf2 radical, Journal of Physical Chemistry C, Nanomater Interfaces 121 (2017) 9:5161-5167.

[34] O'Mahony, A.M., Silvester, D.S., Aldous, L., Hardacre. C., Compton, R.G., Effect of water on the electrochemical window and potential limits of room-temperature ionic liquids. Journal of Chemical Engineering Data 53 (2008) 2884-2891.

[35] Sanchez-Ramirez, N., Assresahegn, B.D., Belanger, D., Torresi, R.M., A comparison among viscosity, density, conductivity, and electrochemical windows of N-n-butyl-N-methylpyrrolidinium and triethyl-n-pentylphosphoniumbis(fluorosulfonyl) ionic liquids and the analogues containing bis(trifluoromethylsulfonyl)imide anion. Journal of Chemical Engineering Data 62 (2017) 3437-3444.

[36] Rollet, A-L., Porion, P., Vaultier, M., Billard, I., Deschamps, M., Bessada, C., Jouvensal, L., Anomalous diffusion of water in [BMIM]{TFSI] room-temperature ionic liquid. Journal of Physical Chemistry B 111 (2007) 11888-11891.

[37] Saihara, K., Yoshimura, Y., Ohta, S., Shimizu, A., Properties of water confined in ionic liquids. Scientific Reports 5 (2015) 10619-10628.

[38] Schmidt, V.M., Ianniello, R., Pastor, E., Gonzalez, S., Electrochemical reactivity of ethanol on porous Pt and PtRu; Oxidation/Reduction reaction in 1 M HClO4, Journal of Physical Chemistry 100 (1996) 17901-17908.

[39] Zech, O., Stoppa, A., Buchner, R., Kunz, W., The conductivity of imidazolium based ionic liquids from (248 to 468) K. B. Variation of the Anion. Journal of Chemical Engineering Data 55 (2010) 1774-1778.

[40] Li, W-J., Han, B-X., Tao, R-T., Zhang, Z-F., Zhang, J-L., Measurement and correlation of the ionic conductivity of ionic liquid-molecular solvent solutions. Chinese Journal of Chemistry 25 (2007) 1349-1356.

[41] Leys, J., Wubbenhorst, M., Menon, C., Rajesh, R., Thoen, J., Glorieux, C., Temperature dependence of the electrical conductivity of imidazolium ionic liquids. Journal of Chemical Physics 128 (2008) 064509.

[42] Widegren, J.A, Saurer, E.M., Marsh, K.N., Magee, J.W., Electrolytic conductivity of four imidazolium based room-temperature ionic liquids the effect of a water impurity, The Journal of Chemical Thermodynamics 37 (2005) 6: 569-575.

[43] Zhang, Q-G., Sun, S-S., Pitula, S., Liu, Q-S., Welz-Biermann, U., Zhang, J-J. Electrical conductivity of solutions of ionic liquids with methanol, ethanol, acetonitrile, and propylene carbonate. Journal of Chemical & Engineering Data 56 (2011) 4659-4664.

[44] Tshibangu, P.N., Ndwandwe, S.N., Dikio, E.D., Density, viscosity, and conductivity study of 1-butyl-3-methylimidazolium bromide, International Journal of Electrochemical Science 6 (2011) 2201-2213.

[45] Bukietynska, K., Jezowski-Trzebiatowska, B., Keller, B., Intensity of f-f bands of neodymium chloride alcohol solvates, Journal of Inorganic and Nuclear Chemistry 43 (1981) 5:1065-1070.

[46] Sinha, S.P., Complexes of the Rare Earths, Print, Elsevier, 2013, P. 62.

[47] Kroon, M.C., Buijs, W., Peters, C.J., Witkamp, G-J., Decomposition of ionic liquids in electrochemical processing, Green Chemistry 8 (2006) 241-245.